A time splitting Chebyshev-Fourier spectral method for the time-dependent rotating nonlocal Schrödinger equation in polar coordinates

Hanquan Wang [a], Jing Wang [b], Shaobo Zhang [c,*], Yong Zhang [c]

[a] *School of Statistics and Mathematics, Yunnan University of Finance and Economics, Kunming, Yunnan, 650221, China*
[b] *Science Building 806, Minzu University of China, Beijing, 100081, China*
[c] *Center for Applied Mathematics, Tianjin University, Tianjin, 300072, China*

ARTICLE INFO

ABSTRACT

In this article, we propose a time splitting Chebyshev-Fourier spectral method to compute the dynamics of rotating nonlocal Schrödinger equation in polar coordinates. Since the rotation term is diagonalizable with Fourier spectral method in azimuthal direction, we split the Hamiltonian into a linear part, i.e., the Laplacian and rotation terms, and the nonlinear part. The linear part is discretized by Chebyshev-Fourier spectral method in space and integrated by Crank-Nicolson or exact matrix exponential. The nonlinear part is solved exactly in physical space, and the nonlocal potential, which is defined as convolution $\varphi := U * |\psi|^2$ with a singular kernel U, is computed via Kernel Truncation method with spectral accuracy. Then we construct a high order time splitting spectral method. Our scheme is spectrally accurate in space and of second/fourth order in the temporal direction. Extensive numerical results are presented to confirm the accuracy and efficiency for both the nonlocal potential and the wave function, together with one application to a two-component rotating dipolar Bose-Einstein condensates. In addition, we investigate the rotational symmetry preserving performance by a comprehensive comparison with existing scheme.

Contents

* Corresponding author.
  E-mail addresses: wang_hanquan@hotmail.com (H. Wang), wangjingmuc@163.com (J. Wang), shaobo_zhang@tju.edu.cn (S. Zhang), Zhang_Yong@tju.edu.cn (Y. Zhang).

1. Introduction

Bose-Einstein condensates (BEC), realized in ultracold dilute bosonic gases for the first time in 1995 [2,15,18], opened a new era in atomic physics, molecular physics, optics, and quantum optics for providing a platform to study the macroscopic quantum world. With the observation of quantized vortices [1,16], whose appearance is a mark of the superfluid nature of BEC, the rotating BEC has attracted widespread attention and has been studied extensively. In 2004, Pfau team at Stuttgart University first achieved the condensate of ^{52}Cr gases [23], whose properties are dominated by the anisotropic and long-range magnetic/electric dipole-dipole interaction. The dipolar BEC brings in more abundant phenomena [21,26] and has spurred great excitement in the atomic physics community.

At temperature T much smaller than the critical temperature T_c, the property of rotating dipolar BEC, under the external trapping potential strongly confined in the z-direction, can be described by the complex-valued wave function $\psi(\mathbf{x}, t)$ whose evolution is governed by the two-dimensional Gross-Pitaevskii equation (GPE) [6,11] as follows

$$i\partial_t \psi(\mathbf{x}, t) = \left[-\frac{1}{2}\Delta + V(\mathbf{x}) + \beta|\psi|^2 - \Omega L_z \right] \psi + \lambda \, \varphi \, \psi(\mathbf{x}, t), \quad t > 0, \tag{1.1}$$

$$\varphi(\mathbf{x}, t) = \int_{\mathbb{R}^2} U(\mathbf{x} - \mathbf{y})|\psi|^2(\mathbf{y}, t)\,\mathrm{d}\mathbf{y}, \quad \mathbf{x} \in \mathbb{R}^2, \tag{1.2}$$

$$\psi(\mathbf{x}, 0) = \psi_0(\mathbf{x}), \qquad \mathbf{x} \in \mathbb{R}^2, \tag{1.3}$$

where $\beta, \lambda \in \mathbb{R}$ describe the strength of short-range and long-range interactions respectively, the nonlocal potential φ is defined as the convolution of kernel $U(\mathbf{x})$, representing the fundamental interaction between particles, and the density $\rho := |\psi|^2$. The rotation $L_z = -i(x\partial_y - y\partial_x) = -i\partial_\theta$ is the z-component of the angular momentum and Ω is the corresponding frequency. In Bose-Einstein condensates, $V(\mathbf{x})$ is usually chosen as the harmonic potential, i.e.,

$$V(\mathbf{x}) = \frac{1}{2}\left(\gamma_x^2 x^2 + \gamma_y^2 y^2\right), \tag{1.4}$$

with $\gamma_x, \gamma_y > 0$ being the trapping frequencies in the x and y directions respectively. Under such confining potential, the wave function is fast-decaying and smooth, so is the density.

Some frequently used kernels [6,12] are given below

$$U(\mathbf{x}) := \begin{cases} \frac{1}{2\pi}\frac{1}{|\mathbf{x}|}, & \text{Coulomb,} \\ -\frac{1}{2\pi}\ln|\mathbf{x}|, & \text{Poisson,} \\ -\frac{3}{2}(\partial_{\mathbf{n}_\perp \mathbf{n}_\perp} - n_3^2\nabla_\perp^2)(\frac{1}{2\pi|\mathbf{x}|}), & \text{DDI,} \end{cases} \tag{1.5}$$

with $\nabla_\perp = (\partial_x, \partial_y)^T$, the dipole orientation $\mathbf{n} = (\mathbf{n}_\perp, n_3)^T = (n_1, n_2, n_3)^T$ being a unit vector, $\partial_{\mathbf{n}_\perp} = \mathbf{n}_\perp \cdot \nabla_\perp$ and $\partial_{\mathbf{n}_\perp \mathbf{n}_\perp} = \partial_{\mathbf{n}_\perp}(\partial_{\mathbf{n}_\perp})$. All kernels are singular at the origin and decay either polynomially slow or diverge at the far field, e.g., the Poisson kernel. Actually, these kernels are the Green's function of some differential or pseudo-differential equations. For example, the potential generated by the Poisson kernel $-\frac{1}{2\pi}\ln|\mathbf{x}|$ satisfies the following Poisson equation

$$-\Delta\varphi(\mathbf{x}, t) = \rho(\mathbf{x}, t), \quad \mathbf{x} \in \mathbb{R}^2, \tag{1.6}$$

with the far-field condition

$$\lim_{|\mathbf{x}| \to \infty} \left[\varphi(\mathbf{x}, t) + \frac{C_0}{2\pi}\ln|\mathbf{x}| \right] = 0, \qquad C_0 = \int_{\mathbb{R}^2} \rho(\mathbf{x}, t)\mathrm{d}\mathbf{x}.$$

While the potential corresponding to Coulomb kernel $\frac{1}{2\pi}|\mathbf{x}|^{-1}$ satisfies the square-root of Poisson equation

$$\sqrt{-\Delta}\,\varphi(\mathbf{x},t) = \rho(\mathbf{x},t), \quad \text{with} \lim_{|\mathbf{x}|\to\infty} \varphi(\mathbf{x},t) = 0, \tag{1.7}$$

which is a pseudo-differential equation defined by Fourier integral [12]. The dipole potential, generated by DDI kernel, can be equivalently reformulated as

$$\varphi(\mathbf{x}) = \left(\frac{1}{2\pi|\mathbf{x}|}\right) * [-\frac{3}{2}(\partial_{\mathbf{n}_\perp \mathbf{n}_\perp} - n_3^2\nabla_\perp^2)\rho] := \left(\frac{1}{2\pi|\mathbf{x}|} * \widetilde{\rho}\right)(\mathbf{x}), \tag{1.8}$$

for smooth densities. Therefore, it can be computed via the Coulomb potential with modified density $\widetilde{\rho}$. The DDI with different dipole orientations can be reformulated as

$$\varphi(\mathbf{x}) = \left(\frac{1}{2\pi|\mathbf{x}|}\right) * [-\frac{3}{2}(\partial_{\mathbf{n}_\perp \mathbf{m}_\perp} - n_3 m_3\nabla_\perp^2)\rho], \tag{1.9}$$

where $\mathbf{m} = (\mathbf{m}_\perp, m_3)^T$, $\partial_{\mathbf{m}_\perp} = \mathbf{m}_\perp \cdot \nabla_\perp$ and $\partial_{\mathbf{n}_\perp \mathbf{m}_\perp} = \partial_{\mathbf{n}_\perp}(\partial_{\mathbf{m}_\perp}) = \partial_{\mathbf{m}_\perp}(\partial_{\mathbf{n}_\perp})$.

There is vast literature on mathematical and numerical studies on the dynamics, and we refer to [6,3] for more details. Along the numerical front, the time-splitting Fourier spectral method is one of the most successful methods, and has been successfully adapted to the rotating BEC [13] and dipolar BEC [7]. Bao et al. introduced a rotating Lagrangian coordinate method for the rotating BEC with/without long-range nonlocal potential [11], in which the rotation term vanishes simultaneously. Therefore, it is relatively easy to design a high order time splitting Fourier spectral method therein. Using the rotating Lagrangian coordinate, Besse et al. proposed some high order exponential Runge-Kutta and Lawson methods [14]. However, if one has to switch to original cartesian coordinates, spectral interpolations are inevitably invoked, and the computation efficiency will be bottlenecked if coordinate switches are called multiple times in simulation, even though such inefficiency can be alleviated to some extent by NonUniform FFT (NUFFT) algorithm. Recently, Meng et al. proposed an efficient method for coordinate switch using only FFT/iFFT pairs based on PDE reformulation, which helps alleviate, or even get rid of, the efficiency bottleneck [31].

The nonlocal dipolar potential was first computed by solving Poisson equation with homogeneous Dirichlet boundary conditions using sine spectral method [7]. However, the approximation accuracy of the potential reaches a saturation as mesh size decreases, and such saturation is caused by boundary condition approximation [9,29]. Lack of accurate numerical solvers may result in suspicious artificial oscillations [4], or even significant accuracy lost in the long time dynamics, for example, the quantum turbulence simulation [25]. It is therefore important to incorporate fast and accurate potential solvers to achieve better resolution for long time simulation. In 2017, Tang et al. combined the rotating Lagrangian coordinates with Gaussian-sum method (GauSum) method, one of the fast nonlocal potential solvers, to simulate the dynamics of two-component rotating dipolar BEC [35].

When the trapping potential and convolution kernel function are both isotropic, the rotating nonlocal Schrödinger equation keeps the fully rotational symmetry (see Theorem B.1). It is natural to choose polar coordinates for constructing rotational symmetry-preserving algorithms because the rotation mechanism is described solely in the azimuthal variable. Moreover, the rotation term is diagonalized automatically after applying Fourier pseudospectral method in azimuthal direction. In fact, several numerical methods have been proposed in polar coordinates. In [8], a time-splitting method in polar/cylindrical coordinates (2D/3D) was proposed, which is of spectral accuracy in the azimuthal direction by Fourier pseudospectral method and second/fourth order in the radial direction by finite difference/element method. Later, Bao et al. proposed a time-splitting generalized Laguerre-Fourier-Hermite pseudospectral method in the whole space [10], and Xia et al. improved its stability using scaling and moving techniques to make it much more practical [37].

As the wave function decays fast enough, it is convenient to first truncate the whole space into a bounded disk and impose homogeneous boundary conditions on the wave function. Therefore, in this article, we choose to work in a bounded disk and aim to design an accurate, both spatially and temporally, and efficient numerical method. To this end, there are **three** major challenges ahead.

The *first* challenge is to design an efficient and accurate numerical scheme to approximate the wave function. The most natural way is to first expand the wave function in azimuthal direction by Fourier pseudospectral method, which can be accelerated by discrete Fast Fourier Transform (FFT), and apply the Chebyshev pseudospectral method in radial direction [30]. The rotation term is diagonalized automatically, and Chebyshev pseudospectral method applies readily with ease in the radial direction. For sake of simplicity, we shall name it as Chebyshev-Fourier spectral method (CFSM) hereafter.

The *second* challenge lies in the nonlocal potentials evaluation. Since the interaction kernel U and its Fourier transform are both singular at the origin, we need to treat the singularity with special care. It is clear that simple discretization in either physical or phase space shall result in poor accuracy. Actually, there have been some successful fast solvers proposed, including the Kernel Truncation method (KTM) [36], Nonuniform FFT method (NUFFT) [24], Gaussian-sum method (GauSum) [19] and Anisotropic Truncated Kernel method (ATKM) [22], among which KTM is the most simple method with easy adaptations to general kernels and geometries [17]. As is reported in [5], to compute the potential φ on a rectangular domain, we first cut off the interaction kernel U outside a larger isotropic circular domain, and then compute the potential generated by the truncated kernel in Fourier space using trapezoidal rule to achieve spectral accuracy. While, in polar coordinates, it is quite challenging to construct an accurate potential solver with feasible efficiency based on KTM and CFSM.

The *last* challenge is to construct a high order numerical integrator in the temporal direction and combine the CFSM and nonlocal potential solver. As the rotation term is diagonalized with Fourier spectral method in azimuthal direction, it is possible to group the Laplacian and rotation terms together as the linear subproblem, and we leave the rest part of the Hamiltonian as the nonlinear subproblem. Each subproblem can be solved efficiently and accurately in either phase space, i.e., the Fourier phase space for the

linear subproblem, or the physical space for the nonlinear subproblem. Then we apply a high order operator splitting scheme [6,38] to compute the dynamics.

The rest of the paper is organized as follows: In Section 2, we propose the Chebyshev-Fourier spectral method to discretize the wave function, adapt KTM on the disk based on the CFSM approximation to compute the nonlocal potential, and construct a high order time splitting Chebyshev-Fourier spectral method for dynamics. In Section 3, we present extensive numerical results to confirm the spectral accuracy and efficiency for the wave function and nonlocal potential, compare the symmetry preserving capabilities of our method and existing well-known method, and apply it to a two-component rotating dipolar BEC. Finally, some conclusions are drawn in Section 4, together with four related theorems provided in the Appendix A-C.

2. Numerical algorithm

In the presence of a confining potential $V(\mathbf{x})$, the wave function $\psi(\mathbf{x})$ (also the density $\rho(\mathbf{x})$) is usually smooth and decays exponentially fast. Therefore, it is reasonable to truncate the whole space $\mathbb{R}^2$ into a bounded domain. As the rotation term is diagonalized in polar coordinates simultaneously, it is natural to choose a disk-shaped domain, and we denote it as $\mathcal{B}_R := \{\mathbf{x} \in \mathbb{R}^2 \big| |\mathbf{x}| \le R\}$ with radius $R > 0$. The wave function and density are both assumed to be compactly supported (numerically) inside the disk $\mathcal{B}_R$, i.e., $\operatorname{supp}(\psi) \subset \mathcal{B}_R$. For the sake of simplicity, hereafter we shall just omit the time variable t if the discussion is just on spatial discretization.

2.1. Chebyshev-Fourier spectral method

To approximate the wave function $\psi(\mathbf{x})$ on the disk, we choose to work in polar coordinates (r, θ) and propose the Chebyshev-Fourier spectral method. We first approximate it in the azimuthal direction by applying the Fourier spectral method

$$\psi(\mathbf{x}) \approx \sum_{k=-N_\theta/2}^{N_\theta/2-1} \widehat{\psi}_k(r) e^{ik\theta}, \quad \mathbf{x} \in \mathcal{B}_R, \tag{2.10}$$

where the Fourier coefficients are defined as

$$\widehat{\psi}_k(r) = \frac{1}{2\pi} \int_0^{2\pi} \psi(r,\theta) e^{-ik\theta} \, \mathrm{d}\theta. \tag{2.11}$$

In the radial direction, we use Chebyshev spectral method [34] to approximate the Fourier coefficients $\widehat{\psi}_k(r)$ on $[0, R]$. By a change of variable $r = R(1-u)/2$, we have $\widehat{\psi}_k(r) = \widetilde{\psi}_k(u)$ and it is well approximated by Chebyshev series

$$\widehat{\psi}_k(r) = \widetilde{\psi}_k(u) \approx \sum_{l=0}^{N_r} \widehat{\psi}_{kl} \, T_l(u), \quad u \in [-1,1], \tag{2.12}$$

with $T_l(u) = \cos(l \arccos(u))$ being the l-th order Chebyshev polynomial. The coefficients $\widehat{\psi}_{kl}$ are determined as

$$\widehat{\psi}_{kl} = \langle T_l, T_l \rangle^{-1} \langle \widetilde{\psi}_k, T_l \rangle = c_l^{-1} \langle \widetilde{\psi}_k, T_l \rangle, \tag{2.13}$$

where $\langle f, g \rangle := \int_{-1}^1 f(u)g(u)/\sqrt{1-u^2} \, \mathrm{d}u$ is the weighted inner product in $\mathcal{L}^2([-1,1])$, and $c_l := \langle T_l, T_l \rangle, c_0 = \pi, c_l = \pi/2, l = 1, \ldots, N_r$. The inner product is evaluated by the Chebyshev-Gauss-Radau (CGR) quadrature

$$\int_{-1}^1 f(u) \, T_l(u) \frac{1}{\sqrt{1-u^2}} \, \mathrm{d}u = \sum_{i=0}^{N_r} f(u_i) \, T_l(u_i) \, w_i, \ \forall \ f \in \mathcal{P}_{N_r}(u), \ l = 0, \ldots, N_r, \tag{2.14}$$

where nodes $u_i = \cos(\pi(2i+1)/(2N_r+1))$, $i = 0, \ldots, N_r$ with $u_0 \to 1$ $(N_r \to \infty)$, $u_{N_r} = -1$, and weights $w_i = \pi s_i/(2N_r + 1)$ with $s_{N_r} = 1$ and $s_i = 2$ otherwise. Correspondingly, in the radial direction, the CGR nodes read as

$$r_i = \frac{R}{2}(1-u_i) = \frac{R}{2}\left(1 - \cos(\pi \frac{2i+1}{2N_r+1})\right), \quad i = 0, \ldots, N_r, \tag{2.15}$$

with $r_0 = R/2(1 - \cos(\pi/(2N_r+1))) \to 0$ $(N_r \to \infty)$, and $r_{N_r} = R$ sitting on the boundary. The Chebyshev coefficients (2.13) are approximated as

$$\widehat{\psi}_{kl} \approx c_l^{-1} \sum_{i=0}^{N_r} \omega_i \widehat{\psi}_k(r_i) \cos\left(\frac{\pi l(2i+1)}{2N_r+1}\right),$$

$$\approx \widetilde{\psi}_{kl} := c_l^{-1} \sum_{i=0}^{N_r} \omega_i \left(\frac{1}{N_\theta} \sum_{j=0}^{N_\theta-1} \psi(r_i, \theta_j) e^{-ik\theta_j}\right) \cos\left(\frac{\pi l(2i+1)}{2N_r+1}\right), \tag{2.16}$$
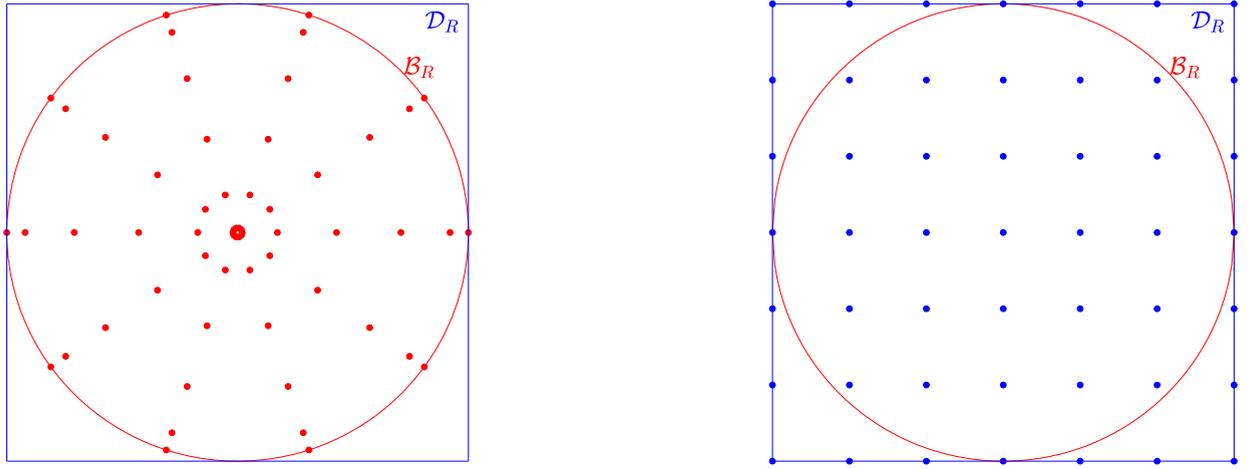
Fig. 1. Schematic diagrams of grid distribution in circular (left) and square domain (right).

with $\theta_j = 2\pi j / N_\theta$, $j = 0, \ldots, N_\theta - 1$ distributed equally in $[0, 2\pi]$. To compute the Chebyshev-Fourier coefficients $\widetilde{\psi}_{kl}$ from grid function $\psi_{ij} := \psi(r_i, \theta_j)$, we need to evaluate the above double summation efficiently via fast algorithm. The inner summation can be accelerated by discrete Fast Fourier Transform (FFT) within $O(N_r N_\theta \log N_\theta)$ operations, while the outer summation (with respect to index i) can actually be accelerated by the fast Discrete Cosine Transform (DCT) within $O(N_\theta N_r \log N_r)$ operations. By tensor product of uniform azimuthal grid $\{\theta_j\}$ and CGR radial grid $\{r_i\}$, we generate the mesh grid (see Fig. 1) as

$$\mathcal{T} := \{r_i(\cos(\theta_j), \sin(\theta_j)) \in \mathcal{B}_R, \ i = 0, \ldots, N_r, \ j = 0, \ldots, N_\theta - 1\}. \tag{2.17}$$

We then construct an interpolating Chebyshev-Fourier series on mesh grid $\mathcal{T}$ as

$$\psi(\mathbf{x}) \approx P(r, \theta) := \sum_{k=-N_\theta/2}^{N_\theta/2-1} \left(\sum_{l=0}^{N_r} \widetilde{\psi}_{kl} \, T_l \left(1 - \frac{2r}{R}\right) \right) e^{ik\theta}, \qquad \mathbf{x} \in \mathcal{B}_R, \tag{2.18}$$

which is, in fact, an interpolation polynomial of order $N_r + 1$ and N_θ in the radial and azimuthal variables respectively. Using such polynomial, we can approximate the Laplacian and rotating function on mesh grid $\mathcal{T}$ as follows

$$(\Delta\psi)(\mathbf{x}) \approx \left(\partial_{rr} + \frac{1}{r}\partial_r + \frac{1}{r^2}\partial_{\theta\theta}\right) P(r, \theta), \tag{2.19}$$

$$(L_z\psi)(\mathbf{x}) \approx (-i\partial_\theta P)(r, \theta) = \sum_{k=-N_\theta/2}^{N_\theta/2-1} \left(\sum_{l=0}^{N_r} \widetilde{\psi}_{kl} \, T_l \left(1 - \frac{2r}{R}\right) \right) k \, e^{ik\theta}. \tag{2.20}$$

Actually, we can approximate the function and its derivatives at any given target points, including the grid and off-grid points. For example, for $\mathbf{x} \notin \mathcal{T}$, we can calculate $\psi(\mathbf{x})$ by computing $P(r, \theta)$ using its polar coordinates. However, the origin $\mathbf{0}$ corresponds to *infinitely many* points in polar coordinates, i.e., $r = 0, \theta \in [0, 2\pi]$, and then evaluating P *does not* guarantee one unique value. As pointed out by Shen [33,34], *essential pole conditions* for nonzero Fourier modes hold, i.e., $\widehat{\psi}_k(0) = 0, \forall k \neq 0$. Therefore, to obtain the function value at the origin, we choose to nullify all the nonzero modes and only consider the zero Fourier mode interpolation, i.e.,

$$\psi(\mathbf{0}) \approx \sum_{l=0}^{N_r} \widetilde{\psi}_{0l} \, T_l(1) = \sum_{l=0}^{N_r} \widetilde{\psi}_{0l}. \tag{2.21}$$

Polar coordinates bring in complexity for the evaluation of convolution-type nonlocal potentials due to lack of coordinates separability, compared with Cartesian coordinates. To address the challenge, we design a fast algorithm in subsection 2.2 by combining Chebyshev-Fourier spectral method and Kernel Truncation method together with a coordinates switch. In addition, the transformation of polar coordinates brings the singularity in Laplacian operator at $r = 0$, but this singularity at the origin is non-essential. To deal with the singularity, we adopt Chebyshev-Gauss-Radau nodes in radial direction to exclude the singular point $r = 0$, and further construct accurate numerical methods for solving the dynamics of Schrödinger equation in subsection 2.3.

2.2. Chebyshev-Fourier-Kernel Truncation method

In fact, after applying the differential operator $\mathcal{L} = \partial_{\mathbf{n}_\perp \mathbf{n}_\perp} - n_3^2 \nabla_\perp^2$ to $\rho(\mathbf{x})$, the DDI can be reduced to convolution with Coulomb kernel. Therefore, in this subsection, we shall focus on the convolution of kernel $U(\mathbf{x})$, which might be singular at the origin and/or far-field, and fast-decaying smooth density $\rho(\mathbf{x})$. To compute the nonlocal potential on the disk, we have
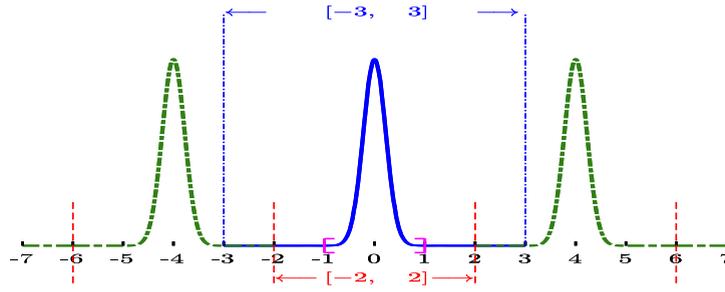
Fig. 2. Schematic diagram of the twofold zero-padding (assume $R = 1$). The solid-blue curve is the Fourier series approximation over $[-2, 2]$ and dotted-green curve corresponds to the periodic extension over the whole space. (For interpretation of the colors in the figure(s), the reader is referred to the web version of this article.)

$$\varphi(\mathbf{x}) = (U * \rho)(\mathbf{x}) = \int_{\mathbb{R}^2} U(\mathbf{x} - \mathbf{y})\rho(\mathbf{y})d\mathbf{y} = \int_{\mathcal{B}_R} U(\mathbf{x} - \mathbf{y})\rho(\mathbf{y})d\mathbf{y}, \quad \mathbf{x} \in \mathcal{B}_R. \tag{2.22}$$

By a change of variable $\mathbf{z} = \mathbf{x} - \mathbf{y}$, we have

$$\varphi(\mathbf{x}) = \int_{\mathbf{x} + \mathcal{B}_R} U(\mathbf{y})\rho(\mathbf{x} - \mathbf{y})d\mathbf{y}, \quad \mathbf{x} \in \mathcal{B}_R. \tag{2.23}$$

For computing φ at target point $\mathbf{x}$, the exact compact integration domain is $\mathbf{x}$-dependent, i.e., a ball centered at $\mathbf{x}$ with radius R. Since the density vanishes outside $\mathcal{B}_R$, it is easy to check that $\rho(\mathbf{x} - \mathbf{y}) = 0$, $\forall\, \mathbf{x} \in \mathcal{B}_R$, $\forall\, \mathbf{y} \in \mathcal{B}_{2R} \setminus (\mathbf{x} + \mathcal{B}_R)$. Therefore, the above integral can be reformulated as follows

$$\varphi(\mathbf{x}) = \int_{\mathcal{B}_{2R}} U(\mathbf{y})\rho(\mathbf{x} - \mathbf{y})d\mathbf{y}, \quad \mathbf{x} \in \mathcal{B}_R. \tag{2.24}$$

To facilitate the computation of (2.24), it is convenient to utilize the density's finite Fourier series approximation over $\mathcal{B}_{3R}$ as $(\mathbf{x} - \mathbf{y}) \in \mathcal{B}_{3R}$, $\forall\, \mathbf{x} \in \mathcal{B}_R, \mathbf{y} \in \mathcal{B}_{2R}$, because $\rho(\mathbf{x})$ is a fast-decaying and smooth function. As is well-known, the finite Fourier series suits best for rectangular domain, e.g., the circumscribing square of disk $\mathcal{B}_R$, which is denoted as $\mathcal{D}_R := [-R, R]^2$, with uniform mesh grid, please refer to Fig. 1 for an illustrative description. The domain $\mathcal{D}_R$ is discretized in each spatial direction as $x_p = -R + p\frac{2R}{N_x}$ and $y_q = -R + q\frac{2R}{N_y}$, and the uniform mesh grid is denoted as

$$\mathcal{T}_{rect} := \{(x_p, y_q) \in \mathcal{D}_R, p = 0, 1, \dots, N_x - 1, q = 0, 1, \dots, N_y - 1\}. \tag{2.25}$$

The Fourier series naturally extends periodically over the whole space, and fortunately, the periodic extension of Fourier series derived on $\mathcal{D}_{2R}$ approximates the density over $\mathcal{B}_{3R}$ with spectral accuracy. An intuitive explanation is shown by a one-dimensional sketch in Fig. 2, where the solid-blue curve represents Fourier series approximation over two-fold padded domain and the dotted-green curve denotes the periodic extension of the solid-blue Fourier approximation. From Fig. 2, we can see clearly that the Fourier series approximation on a twofold domain *matches* the density $\rho(\mathbf{x})$ over a threefold domain within spectral accuracy. Similarly, we can draw the same conclusions for a three-dimensional ball-shaped domain.

To obtain Fourier series approximation over $\mathcal{D}_{2R}$, we first carry out a twofold zero-padding of density by setting $\rho(\mathbf{x}) = 0, \forall\, \mathbf{x} \in \mathcal{D}_{2R} \setminus \mathcal{B}_R$. Then we construct a Fourier series from the uniform mesh grid of $\mathcal{D}_{2R}$ following the standard Fourier pseudospectral method [34]. To be exact, the density is well approximated by the following finite Fourier series

$$\rho(\mathbf{x}) \approx \sum_{\mathbf{k} \in \Lambda} \widehat{\rho}_{\mathbf{k}} e^{i\,\mathbf{k}\cdot\mathbf{x}}, \qquad \mathbf{x} \in \mathcal{D}_{2R}, \tag{2.26}$$

with index set $\Lambda := \{\mathbf{k} = \frac{\pi}{2R}(k_i, k_j), k_i = -N_x, \dots, N_x - 1, k_j = -N_y, \dots, N_y - 1\}$. The Fourier coefficients are given by

$$\widehat{\rho}_{\mathbf{k}} = \frac{1}{(4R)^2} \int_{\mathcal{D}_{2R}} \rho(\mathbf{x}) e^{-i\mathbf{k}\cdot\mathbf{x}} d\mathbf{x}, \tag{2.27}$$

which is well approximated by trapezoidal rule and accelerated by Fast Fourier Transform within $O(N \log N)$ operations with $N = 4N_x N_y$ being the total number of grid points. Plugging Eq. (2.26) back into Eq. (2.24), we arrive

$$\varphi(\mathbf{x}) \approx \sum_{\mathbf{k} \in \Lambda} \widehat{\rho}_{\mathbf{k}} \left(\int_{\mathcal{B}_{2R}} U(\mathbf{y}) e^{-i\mathbf{k}\cdot\mathbf{y}} d\mathbf{y} \right) e^{i\,\mathbf{k}\cdot\mathbf{x}} := \sum_{\mathbf{k} \in \Lambda} \widehat{\rho}_{\mathbf{k}}\, \widehat{U_B}(\mathbf{k})\, e^{i\,\mathbf{k}\cdot\mathbf{x}}, \quad \mathbf{x} \in \mathcal{B}_R. \tag{2.28}$$

The Fourier transform of the kernel $\widehat{U_B}(\mathbf{k})$ is given explicitly

$$\widehat{U_B}(\mathbf{k}) := \int_{B_{2R}} U(\mathbf{y})e^{-i\mathbf{k}\cdot\mathbf{y}}\mathrm{d}\mathbf{y}. \tag{2.29}$$

Due to the Paley-Wiener theorem, we know that $\widehat{U_B}(\mathbf{k})$ is smooth and is not singular any more. For symmetric convolution kernel, the above Fourier transform can be integrated analytically or exact up to machine precision by some high-order numerical quadratures. For example, the Fourier transform of the 2D Coulomb kernel (Eq. (1.5)) is given explicitly

$$\widehat{U_B}(\mathbf{k}) = 2\pi \int_0^{2R} J_0(kr)U(r)r\mathrm{d}r = R(\pi J_1(2Rk)\,\mathrm{SH}_0(2Rk) + J_0(2Rk)(2 - \pi\,\mathrm{SH}_1(2Rk))), \tag{2.30}$$

where $k = |\mathbf{k}|$, J_0, J_1 are Bessel functions of the first-kind with index 0 and 1, and $\mathrm{SH}_0, \mathrm{SH}_1$ are Struve functions of order 0 and 1, respectively. For more examples, we refer the readers to [5].

Once $\widehat{U_B}(\mathbf{k})$ is at hand, we can easily calculate the potential $\varphi(\mathbf{x})$ by summing up the Fourier series Eq. (2.28). To compute φ on $\mathcal{T} \subset \mathcal{B}_R$ from the density's grid value, i.e., $\{\rho_{ij} := \rho(\mathbf{x}_{ij}) | \mathbf{x}_{ij} = (r_i\cos(\theta_j), r_i\sin(\theta_j)) \in \mathcal{T}\}$, we can calculate the Fourier transform of the density, i.e., $\hat\rho(\mathbf{k})$, from its zero-padded value from $\mathcal{T}_{rect}$, which can be implemented efficiently by FFT. From nonuniform grid $\mathcal{T}$, we utilize the interpolating Chebyshev-Fourier series (Eq. (2.16)-(2.18)) to obtain ρ_{pq} on uniform grid $\mathcal{T}_{rect}$ by a simple substitution of ρ_{ij} for ψ_{ij}.

To compute $\widetilde\rho_{kl}$ via Eq. (2.16), we can accelerate the double summation by FFT (inner) and DCT (outer) within $\mathcal{O}(N_\theta N_r \log(N_\theta N_r))$ operations. To interpolate $\rho(\mathbf{x})$ at uniform mesh grid $\mathcal{T}_{rect}$, we first reformulate Eq. (2.18) as the following Fourier series

$$P(r,\theta) = \frac{1}{2} \sum_{k=-N_\theta/2}^{N_\theta/2-1} \left(\sum_{l=-N_r}^{N_r} \widetilde\rho_{k|l|}\, e^{il\cdot\arccos(1-\frac{2r}{R})} + \widetilde\rho_{k0} \right) e^{ik\theta}, \tag{2.31}$$

and then evaluate the above series at $\mathcal{T}_{rect}$, which corresponds to nonuniform grid in polar coordinates, via NUFFT. The NUFFT can accelerate such summation and reduce the computational costs within $\mathcal{O}(N_{\mathrm{disk}} + N_{\mathrm{rect}}\log N_{\mathrm{rect}})$ flops where $N_{\mathrm{disk}} = N_r N_\theta$, $N_{\mathrm{rect}} = N_x N_y$ are the total number of grid points in the disk and rectangular domain respectively. The Fourier transform $\hat\rho_{\mathbf{k}}$ (Eq. (2.28)) is readily available by the Fourier spectral method. In particular, to evaluate DDI via Coulomb potential, we compute $\rho' := \mathcal{L}\rho$ by differentiating the density in Fourier space, which is implemented on mesh grid $\mathcal{T}_{rect}$ via FFT.

In the last step, to compute the nonlocal potential $\varphi(\mathbf{x})$ on nonuniform mesh grid $\mathcal{T}$ by Eq. (2.28), we again apply NUFFT to help reduce the computational costs within $\mathcal{O}(N_{\mathrm{rect}} + N_{\mathrm{disk}}\log N_{\mathrm{disk}})$ flops.

Algorithm 1 Chebyshev-Fourier-KTM for computing nonlocal interactions φ.

Require: Given a smooth and fast-decaying function ρ at non-uniform grids $\mathcal{T}$.
Require: Pre-compute $\widehat{U_B}(\mathbf{k}), \mathbf{k} \in \Lambda$.
1: Compute $\widetilde\rho_{kl}$ by Eq. (2.16) via FFT and DCT.
2: Interpolate the density at uniform mesh grid $\mathcal{T}_{rect}$ by Eq. (2.31) via NUFFT.
3: Compute $\hat\rho_{\mathbf{k}}$ via FFT on doubly padded density.
4: Compute $\widehat{U_B}(\mathbf{k})\,\hat\rho_{\mathbf{k}}$ by pointwise multiplication.
5: Compute the potential φ on nonuniform mesh grid $\mathcal{T}$ by Eq. (2.28) via NUFFT.

Remark 2.1. The Chebyshev-Fourier-KTM is an efficient and spectrally accurate numerical algorithm, whose detailed error estimate is presented in Appendix C.

Remark 2.2. In this subsection, we proved that a **twofold** zero-padding of the density is both **sufficient** and **optimal** to guarantee the spectral accuracy of φ on $\mathcal{B}_R$. While for nonlocal potential φ on $\mathcal{D}_R$, one was suggested to carry out a *fourfold* zero-padding to overcome the integrand's oscillations in KTM [36], and it is proved by Liu et al. [28] that fourfold is redundant and **threefold** is sufficient for spectral accuracy.

Remark 2.3. In fact, following the same arguments, we can prove that twofold zero-padding is sufficient and optimal for ball-shaped domain, which is of great importance in terms of storage and efficiency for practice simulations. Compared with the KTM [28], the minimal storage requirement is around $2^d N$ instead of $3^d N$ with N being the total number of grid points.

2.3. Time splitting Chebyshev-Fourier method

To compute Eq. (1.1)-(1.3), we first truncate the whole space into a bounded disk $\mathcal{B}_R$, which is large enough such that errors coming from the truncation are negligible, then we impose homogeneous Dirichlet boundary conditions on the wave function.

We choose a time step $\Delta t > 0$ and denote $t_n = n\Delta t$, $n = 0, 1, \dots$. To evolve from t_n to t_{n+1}, we choose to apply the operator splitting method. First, we solve the linear equation

$$i\partial_t\psi(\mathbf{x},t) = \left[-\frac{1}{2}\left(\partial_{rr} + \frac{1}{r}\partial_r + \frac{1}{r^2}\partial_{\theta\theta}\right) + i\Omega\partial_\theta\right]\psi(\mathbf{x},t), \quad t_n < t < t_{n+1}, \tag{2.32}$$

for a time step, then we compute the nonlinear equation

$$i\partial_t \psi(\mathbf{x},t) = \left[V(\mathbf{x}) + \beta |\psi|^2(\mathbf{x},t) + \lambda\,\varphi(\mathbf{x},t) \right] \psi(\mathbf{x},t), \quad t_n < t < t_{n+1}, \tag{2.33}$$

for another step.

It is easy to check that Eq. (2.33) keeps the density unchanged, i.e., $\rho(\mathbf{x},t) \equiv \rho(\mathbf{x},t_n)$, and the nonlocal potential also remains unchanged. Therefore, the nonlinear equation is reduced as follows

$$i\partial_t \psi(\mathbf{x},t) = \left[V(\mathbf{x}) + \beta |\psi|^2(\mathbf{x},t_n) + \lambda\,\varphi(\mathbf{x},t_n) \right] \psi(\mathbf{x},t), \quad t_n < t < t_{n+1}, \tag{2.34}$$

and it is integrated exactly as

$$\psi(\mathbf{x},t) = e^{-i\left(V(\mathbf{x}) + \beta |\psi(\mathbf{x},t_n)|^2 + \lambda\varphi(\mathbf{x},t_n) \right)\,(t-t_n)} \psi(\mathbf{x},t_n), \quad \forall t \in [t_n, t_{n+1}]. \tag{2.35}$$

For the linear equation (2.32), we can integrate in time direction either numerically or analytically. Plugging in the finite Fourier series (2.10), we obtain

$$i\partial_t \widehat{\psi}_k(r,t) = \left[-\frac{1}{2}\left(\partial_{rr} + \frac{1}{r}\partial_r - \frac{k^2}{r^2} \right) - k\,\Omega \right] \widehat{\psi}_k(r,t), \quad 0 < r < R, \tag{2.36}$$

for $k = -N_\theta/2, \ldots, N_\theta/2 - 1$ with boundary conditions $\widehat{\psi}_k(R,t) = 0$. As stated earlier, the radial interval is discretized by Chebyshev-Gauss-Radau points (CGR) (2.15), where the singularity point ($r = 0$) is excluded, and the wave function and its derivatives are well approximated by Chebyshev collocation method [34]. The right hand side is computed as $A_k \widehat{\Psi}_k$, where $\widehat{\Psi}_k := \widehat{\psi}_k(\{r_i\}) \in \mathbb{C}^{N_r \times 1}$ is a column vector and the matrix $A_k \in \mathbb{C}^{N_r \times N_r}$ consists of differentiation ($\partial_r/r, \partial_{rr}$) and multiplication ($-k^2/r^2$ and $k\Omega$) information. Note that A_k remains unchanged for each fixed Fourier mode and the size N_r is usually small. Therefore, it is convenient to precompute them once for all in practice for better efficiency with $\mathcal{O}(N_\theta N_r^2)$ memory storage.

With Chebyshev-Fourier spectral approximation in space, the semi-discrete discretization of Eq. (2.36) reads as

$$i\partial_t \widehat{\Psi}_k(t) = A_k \widehat{\Psi}_k(t), \quad k = -N_\theta/2, \ldots, N_\theta/2 - 1. \tag{2.37}$$

To advance from t_n to t_{n+1}, we apply the following Crank-Nicolson (CN) approximation

$$\frac{i}{\Delta t}\left(\widehat{\Psi}_k^{n+1} - \widehat{\Psi}_k^n \right) = \frac{1}{2} A_k \left(\widehat{\Psi}_k^{n+1} + \widehat{\Psi}_k^n \right), \tag{2.38}$$

where $\widehat{\Psi}_k^n \approx \widehat{\Psi}_k(t_n)$ is the numerical approximation of $\widehat{\Psi}_k(\cdot)$ at time t_n. The above method is second order in time and spectrally accurate in space, and we name it as Chebyshev-Fourier-Crank-Nicolson scheme (**ChebCN** for short).

Remark 2.4. For a fixed Fourier index k, noticing the boundary conditions $\widehat{\psi}_k(r_{N_r}, t) = \widehat{\psi}_k(R,t) = 0$, the ChebCN system (2.38) has N_r unknown variables, i.e., $\left\{ \widehat{\psi}_k^{n+1}(r_0), \widehat{\psi}_k^{n+1}(r_1), \cdots, \widehat{\psi}_k^{n+1}(r_{N_r-1}) \right\}$, and the number of equations is N_r too. That is to say, the degrees of freedom and number of equations matches. Numerically, equation (2.38) is solvable for small time steps.

The differentiation matrix is time-independent, and therefore one may integrate Eq. (2.37) directly

$$\widehat{\Psi}_k^{n+1} = e^{-i\Delta t\, A_k} \widehat{\Psi}_k^n, \tag{2.39}$$

where the matrix exponentials are computed at ease in MATLAB using "expm". Different from ChebCN, the above method is exact in time and we name it as Chebyshev-Fourier-Exact method (**ChebExact**) hereafter. Similarly, for fixed time step Δt and N_r, the matrix exponential ($e^{-i\Delta t A_k}$) remains unchanged for each Fourier mode, we can precompute them once for all for sake of efficiency.

In practice, we may apply the classical second order Strang splitting scheme. That is, from t_n to t_{n+1}: (i) solve Eq. (2.32) for a half step $\Delta t/2$ with initial data from time t_n; (ii) compute Eq. (2.33) for one step with initial data obtained from (i); (iii) solve Eq. (2.32) for a half step $\Delta t/2$ with initial data computed from (ii). Here, for the linear equation (2.32), we may apply either ChebCN or ChebExact method.

Compared with the ADI method proposed in Cartesian coordinates [13], it is relative easier in polar coordinates to construct a high order scheme based on the operator splitting method using ChebExact (2.39) scheme, since the Hamiltonian can be split into the linear part, i.e., $-\Delta/2 - \Omega L_z$, and nonlinear part, i.e., $V + \beta |\psi|^2 + \lambda\varphi$, and each part can be solved accurately and efficiently in either Fourier or physical space. Here, using ChebExact scheme (2.39) and the exact integration (2.35), we propose a **fourth-order** Chebyshev-Fourier spectral method based on the Yoshida scheme [3,38], and shall denote it as **ChebYoshida** scheme hereafter. Similarly, we can easily construct numerical algorithms of sixth order or even higher order in time. Such method is also termed as compact operator splitting method as it only involves two operators [31].

Remark 2.5. Under certain circumstances in physical experiments, the wave function is assumed to be supported in a cylindrical or spherical region, and we can naturally extend our methods with ease to simulate the dynamics. To be exact, in cylindrical domain, one may apply Chebyshev-Fourier spectral method in the polar coordinates (r, θ) and Fourier spectral method in the z-direction to approximate the wave function (density). In spherical domain, we shall expand the wave function with spherical harmonics in the azimuthal and zenith variables (θ, ϕ) and Chebyshev spectral method in the radial direction. The nonlocal potential can be dealt with

Kernel Truncation method in a similar way by using such spectral methods and NUFFT algorithm. High order time splitting method readily applies without too many modifications. For sake of simplicity, we choose not to provide details in cylindrical or spherical case in this paper and shall leave them in some future work.

Remark 2.6. Our method is spectrally accurate in space, and it is easier to construct a high order scheme in time with operator splitting scheme. However, if energy preservation is of essential importance in simulation, the operator splitting method needs further investigations. We refer the readers to [20] for arbitrarily higher-order mass and energy preserving scheme, where the finite element methods based on the scalar auxiliary variable (SAV) formulation is utilized.

Remark 2.7. If the initial data is not smooth, we refer to Li's work [27,32]. They proposed the low-regularity exponential-type integrators for 1D cubic nonlinear Schrödinger equation, especially the method of [32] has second-order convergence in L_2 norm in time for initial data strictly below H^2.

3. Numerical results

In this section, we shall first present numerical results to confirm the efficiency and spatial accuracy of Chebyshev-Fourier-KTM for computing different nonlocal interactions. Then, we verify the spatial and temporal accuracy of the time splitting Chebyshev-Fourier spectral method for the dynamics in various setups. Finally, we carry out a comparison on the rotational symmetry conservation with prevailing numerical method, together with one application to a two-component rotating dipolar BEC. In practice, we impose homogeneous Dirichlet boundary conditions for the wave function ψ, and we choose computational domain $\mathcal{B}_R$, grids number $N_x = N_y = 256$ for the computation of nonlocal potential, dipole orientation $\mathbf{m} = \mathbf{n}$ and an isotropic trapping potential, i.e., $V(\mathbf{x}) = \frac{1}{2}|\mathbf{x}|^2$, if not stated otherwise. The algorithms were implemented in Matlab (2019b) and run on a 3.00 GH Intel(R) Xeon(R) Gold 6248R CPU with a 36 MB cache in Ubuntu GNU/Linux.

3.1. Nonlocal potential

In this subsection, we verify the spatial spectral accuracy of the Chebyshev-Fourier-KTM for the Coulomb, Poisson and DDI evaluations.

Example 1. Consider the density $\rho(\mathbf{x}) = e^{-\frac{|\mathbf{x}-\mathbf{a}|^2}{2\sigma^2}}$, $\mathbf{a} = (a_1, a_2)^T \in \mathbb{R}^2$ with $\sigma > 0$. The Coulomb interaction is

$$\varphi(\mathbf{x}) = \frac{\sqrt{\pi}\sigma}{2} I_0\left(\frac{|\mathbf{x}-\mathbf{a}|^2}{2\sigma^2}\right) e^{-\frac{|\mathbf{x}-\mathbf{a}|^2}{2\sigma^2}}, \tag{3.40}$$

where I_0 is the modified Bessel function of order 0, see [5]. The Poisson interaction is

$$\varphi(\mathbf{x}) = -\frac{\sigma^2}{4}\left[E_1(\frac{|\mathbf{x}-\mathbf{a}|^2}{\sigma^2}) + 2\ln(|\mathbf{x}-\mathbf{a}|)\right], \tag{3.41}$$

where $E_1(r) := \int_r^\infty t^{-1}e^{-t}dt$ for $r > 0$ is the exponential integral function [19]. The Dipole-Dipole Interaction is

$$\varphi(\mathbf{x}) = \frac{3\sqrt{\pi}e^{-s}}{4\sigma}[(\mathbf{n}_\perp \cdot \mathbf{m}_\perp)(I_0(s) - I_1(s)) - \frac{2((\mathbf{x}-\mathbf{a}) \cdot \mathbf{n}_\perp)((\mathbf{x}-\mathbf{a}) \cdot \mathbf{m}_\perp)}{\sigma^2}(I_0(s)$$
$$- \frac{1+2s}{2s}I_1(s))] + \frac{3\sqrt{\pi}n_3 m_3 s e^{-s}}{\sigma}\left[I_0(s) - I_1(s) - \frac{I_0(s)}{2s}\right], \tag{3.42}$$

where $s = \frac{|\mathbf{x}-\mathbf{a}|^2}{2\sigma^2}$ and I_1 is the modified Bessel function of order 1, see [5].

Here, we choose $R = 16\sqrt{2}$, $\sigma = \sqrt{1.1}$ and different dipole orientations $\mathbf{n} = (0, -0.8332, 0.55297)^T$, $\mathbf{m} = (0.5, -0.35271, 0.79095)^T$. The numerical errors are calculated in relative maximum norm

$$\mathcal{E}_\infty := \frac{\|\varphi^{N_r,N_\theta} - \varphi^{\text{ext}}\|_\infty}{\|\varphi^{\text{ext}}\|_\infty} = \frac{\max_{\mathbf{x}\in\mathcal{T}}|\varphi^{N_r,N_\theta}(\mathbf{x}) - \varphi^{\text{ext}}(\mathbf{x})|}{\max_{\mathbf{x}\in\mathcal{T}}|\varphi^{\text{ext}}(\mathbf{x})|},$$

where $\varphi^{\text{ext}}, \varphi^{N_r,N_\theta}$ are the exact and numerical solutions respectively. The numerical results are presented in Table 1, from which we can see clearly the spatial spectral accuracy in both radial and azimuthal direction. Fig. 3, which depicts the errors specifically in case $\mathbf{a} = (0,0)^T$, further supports this observation. To show the efficiency, we choose the Coulomb interaction with $\mathbf{a} = (0,0)^T$ and keep the rest parameters the same as above. The computational time and errors are presented in Table 2, from which we can confirm its efficiency performs as expected.

Table 1

Numerical errors of the Chebyshev-Fourier KTM for different nonlocal interactions in Example 1. We fix $N_\theta = 32$ ($N_r = 100$) to investigate the radial (azimuthal) accuracy.

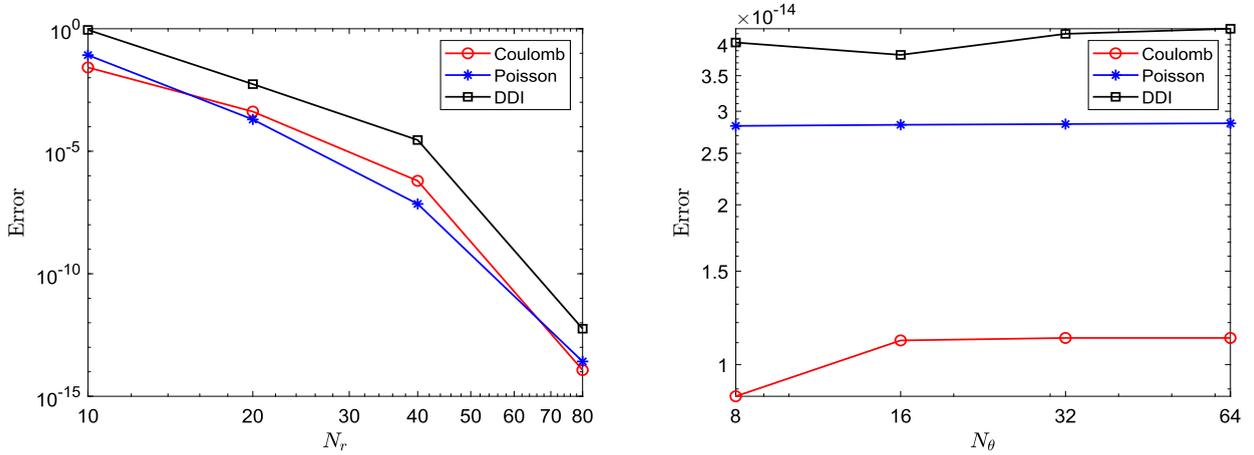| Coulomb interaction					
r	N_r	10	20	40	80
	$\mathbf{a} = (0,0)^T$	2.6280E-02	4.1543E-04	6.1998E-07	1.1765E-14
	$\mathbf{a} = (1,2)^T$	2.6280E-02	4.1543E-04	6.1998E-07	1.1765E-14
θ	N_θ	8	16	32	64
	$\mathbf{a} = (0,0)^T$	8.7195E-15	1.1108E-14	1.1228E-14	1.1228E-14
	$\mathbf{a} = (1,2)^T$	8.6598E-15	1.1108E-14	1.1228E-14	1.1228E-14
Poisson interaction					
r	N_r	10	20	40	80
	$\mathbf{a} = (0,0)^T$	8.3949E-02	1.9816E-04	7.0704E-08	2.6404E-14
	$\mathbf{a} = (1,2)^T$	8.3949E-02	1.9816E-04	7.0704E-08	4.4120E-14
θ	N_θ	8	16	32	64
	$\mathbf{a} = (0,0)^T$	2.8153E-14	2.8289E-14	2.8378E-14	2.8475E-14
	$\mathbf{a} = (1,2)^T$	2.7261E-14	2.8863E-14	4.0722E-14	4.0949E-14
Dipole-Dipole interaction					
r	N_r	10	20	40	80
	$\mathbf{a} = (0,0)^T$	8.9609E-01	5.4862E-03	2.8772E-05	5.7273E-13
	$\mathbf{a} = (1,2)^T$	8.9609E-01	5.4862E-03	2.8772E-05	5.7213E-13
θ	N_θ	8	16	32	64
	$\mathbf{a} = (0,0)^T$	4.0414E-14	3.8303E-14	4.1960E-14	4.2902E-14
	$\mathbf{a} = (1,2)^T$	3.9886E-14	3.7926E-14	4.1846E-14	4.5428E-14

Fig. 3. Errors of Chebyshev-Fourier KTM for nonlocal interactions with $\mathbf{a} = (0,0)^T$ in **Example** 1.

Table 2

Numerical errors and computational time for Coulomb interaction in Example 1.

$N_r \times N_\theta$	N_x (N_y)	$\mathcal{E}_\infty$	Time (s)
10×4	32	2.3869E-01	0.0125
20×8	64	6.8251E-04	0.0419
40×16	128	7.4690E-07	0.1632
80×32	256	1.1765E-14	1.0185

3.2. Accuracy confirmation

In this subsection, we test the spatial and temporal accuracy for ChebCN, ChebExact and ChebYoshida scheme respectively.

Example 2. Consider a rotating dipolar BEC where $\beta = -2, \lambda = 2, \Omega = 1$, the dipole orientation $\mathbf{n} = (0.43, -0.52476, 0.73466)^T$ and the initial value $\psi_0(\mathbf{x}) = e^{-2|\mathbf{x}|^2}(x + iy)$. We choose $R = 16$ and compute the wave function $\psi(\mathbf{x}, T = 0.32)$.

The numerical solution obtained with time step Δt is denoted as $\psi_{\Delta t}^{N_r, N_\theta}$, and we calculate the relative successive error to investigate the convergence. For example, the relative successive error in temporal direction is defined as

Table 3

Spatial and temporal convergence for the dynamics of rotating dipolar BEC in Example 2.

Radial direction					
	N_r	40	80	160	320
ChebCN	$\mathcal{E}_{N_r}$	8.7971E-03	2.6066E-04	6.3298E-08	3.8720E-12
ChebExact	$\mathcal{E}_{N_r}$	8.7972E-03	2.6066E-04	6.3297E-08	1.3918E-12
ChebYoshida	$\mathcal{E}_{N_r}$	8.7972E-03	2.6066E-04	6.3295E-08	6.1492E-12
Azimuthal direction					
	N_θ	8	16	32	64
ChebCN	$\mathcal{E}_{N_\theta}$	3.2840E-05	1.6907E-09	1.7497E-11	7.4848E-13
ChebExact	$\mathcal{E}_{N_\theta}$	3.2840E-05	1.6907E-09	1.7481E-11	7.3624E-13
ChebYoshida	$\mathcal{E}_{N_\theta}$	3.2840E-05	1.6907E-09	1.7491E-11	1.3356E-12
Temporal direction					
	$\Delta t/\Delta t_0$	1	1/2	1/4	1/8
ChebCN	$\mathcal{E}_{\Delta t}$	1.5012E-03	3.1432E-04	7.7407E-05	1.9351E-05
	Ord		2.2558	2.0217	2.0001
ChebExact	$\mathcal{E}_{\Delta t}$	1.0600E-04	2.4567E-05	6.1387E-06	1.5345E-06
	Ord		2.1093	2.0007	2.0002
ChebYoshida	$\mathcal{E}_{\Delta t}$	1.5108E-05	8.3155E-07	5.2765E-08	3.3106E-09
	Ord		4.1834	3.9781	3.9944

$$\mathcal{E}_{\Delta t} := \|\psi_{\Delta t}^{N_r,N_\theta} - \psi_{\Delta t/2}^{N_r,N_\theta}\|_\infty \ / \ \|\psi_{\Delta t/2}^{N_r,N_\theta}\|_\infty, \tag{3.43}$$

where the time step is halved each time and N_r, N_θ are chosen large enough such that errors coming from the spatial discretization are negligible. The corresponding temporal convergence order is defined as follows

$$\text{ord} := \log\left(\mathcal{E}_{\Delta t}/\mathcal{E}_{\Delta t/2}\right)/\log(2). \tag{3.44}$$

The spatial successive errors $\mathcal{E}_{N_r}$ are defined similarly with minor modifications by spectral interpolation in the radial direction. To confirm the spatial convergence, we choose a very small time step $\Delta t = 10^{-5}$ such that the errors coming from the temporal direction are negligible, and choose a large $N_\theta = 64$ to test the radial direction convergence and $N_r = 320$ to verify the azimuthal direction convergence. While, to confirm the temporal convergence, we choose $\Delta t_0 = 3.2 * 10^{-2}$ and set $N_\theta = 64, N_r = 320$ such that errors from the spatial discretization are negligible.

Numerical results are presented in Table 3, from which one can see the *spatial* spectral accuracy in all of the three schemes, and second/second/**fourth** order *temporal* convergence in ChebCN, ChebExact and ChebYoshida respectively. Higher order operator splitting scheme is possible with matrix exponential integration (2.39) and we omit details here for brevity.

3.3. Rotational symmetry

In this subsection, we investigate the rotational symmetry preservation property of three numerical methods, i.e., ChebCN, ChebExact and ADI scheme respectively. For ADI scheme, we choose a rectangular domain $\mathcal{D}_R$ and impose periodic boundary conditions on the wave function.

The rotating nonlocal NLSE (1.1)-(1.3) keeps **rotational symmetry** when both the trapping potential and convolution kernel are isotropic, i.e., $V(\mathbf{x}) = V(|\mathbf{x}|)$ and $U(\mathbf{x}) = U(|\mathbf{x}|)$ (see Theorem B.1). That is, for solutions starting with initial value $\psi_1^0(r,\theta)$ and $\psi_2^0(r,\theta) = \psi_1^0(r,\theta+\alpha)$, $\psi_2(r,\theta,t)$ is also the α-rotation of $\psi_1(r,\theta,t)$ at time t, i.e., $\psi_2(r,\theta,t) = \psi_1(r,\theta+\alpha,t)$. In other words, the system will keep the same rotational symmetry as the initial wave function, e.g., $\psi(\mathbf{x},t)$ is $\boldsymbol{\alpha}$-**rotational symmetry** at any time t if $\psi_0(\mathbf{x})$ is α-rotationally symmetric.

Example 3 *(Spatial discretization)*. For rotating BEC (1.1)-(1.3) ($\Omega = 1$), we compare the wave functions at time T, starting from two different initial wave functions, i.e., $\psi_1^0(r,\theta)$ and its rotation $\psi_2^0(r,\theta) = \psi_1^0(r,\theta+\alpha)$. Consider the following cases

    Case 1: (linear case) $\beta = 0, \lambda = 0$,
    Case 2: (non-dipolar BEC) $\beta = 5, \lambda = 0$,
    Case 3: (dipolar BEC) $\beta = 0, \lambda = 2, \mathbf{n} = (0,0,1)^T$.

The initial wave function is $\psi_1^0(r,\theta) = e^{-(r\cos\theta)^2 - 2(r\sin\theta)^2}$, we compare the difference of $\psi_2(r,\theta,T)$ and $\psi_1(r,\theta+\alpha,T)$ for both the ChebExact and ADI scheme using the following error function

$$\mathcal{E}_{\text{sym}} := \frac{\max_{(r,\theta)\in\mathcal{T}} |\psi_2(r,\theta) - \psi_1(r,\theta+\alpha)|}{\max_{(r,\theta)\in\mathcal{T}} |\psi_2(r,\theta)|}, \tag{3.45}$$

where $\mathcal{T}$ corresponds to uniform Cartesian and polar grid for ADI and ChebExact scheme respectively.
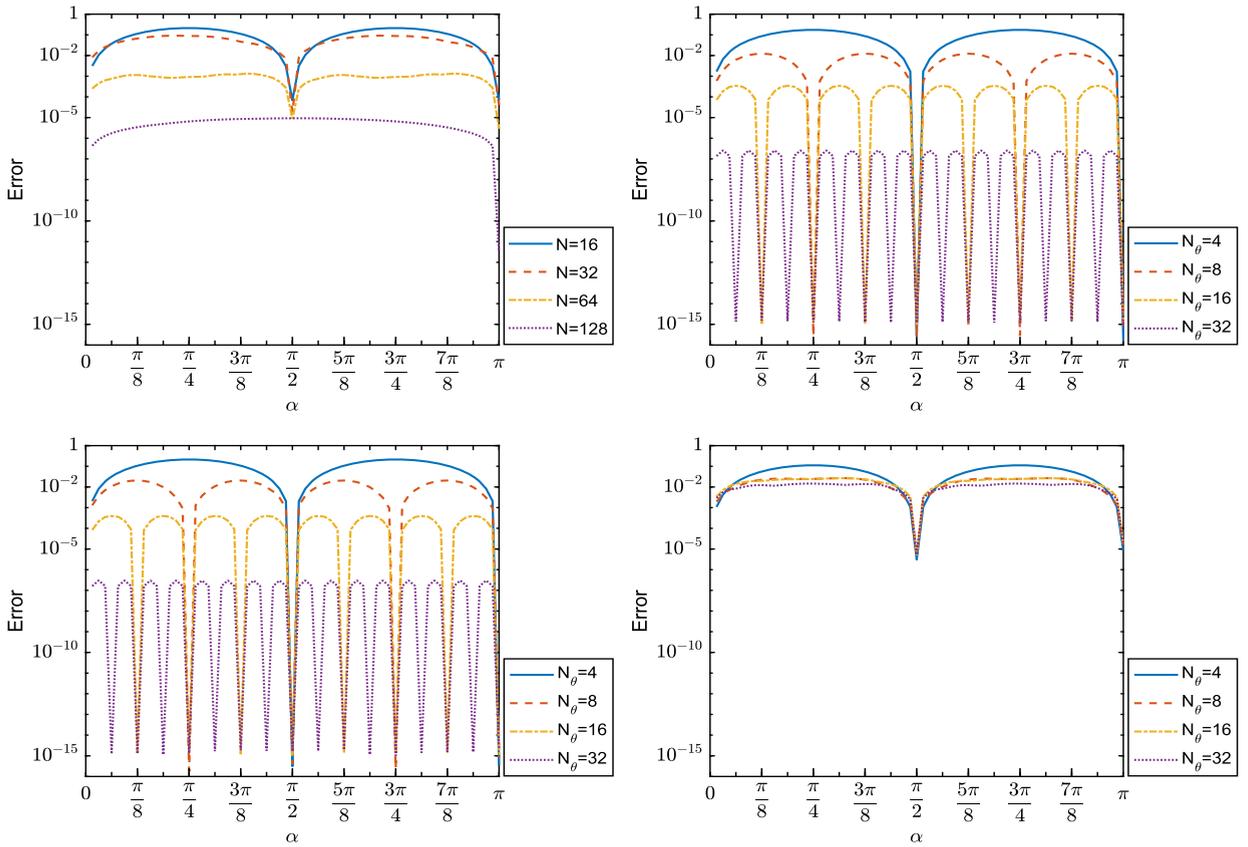
Fig. 4. Errors for **linear** case: ADI (top left), ChebExact (top right), and errors of ChebExact for **non-dipolar** case (bottom left) and **dipolar** case (bottom right) in **Example** 3.

In practice, we choose $\Delta t = 0.01, T = 0.1, R = 16$ with multiple rotation angles $\alpha = k\pi/64, k = 1, 2, \cdots, 64$, and discretize the computational domain with uniform mesh grid $N_x = N_y = N$ for ADI scheme and set $N_r = 10$ in ChebExact scheme. The rotated function $\psi_1(r, \theta + \alpha)$ is evaluated via Fourier/Fourier-Chebyshev spectral interpolation using grid function $\{\psi_1(r_i, \theta_j)\}$. Fig. 4 illustrates errors for the above three cases.

From Fig. 4 and other numerical results not shown here, we conclude that ADI scheme does not keep rotational symmetry for either the linear nor nonlinear case, while the ChebExact scheme keeps rotational symmetry for both linear and non-dipolar case, when the rotational angle α is an integer multiple of mesh length in azimuthal direction. We refer the readers to Theorem B.2 for a rigorous proof. As for the dipolar case, the ChebExact scheme can not keep rotational symmetry, because the nonlocal potential solver is not symmetry preserving.

Example 4 *(Boundary condition).* For rotating BEC (1.1)-(1.3) with parameters $\Omega = 1/3$ and $\lambda = 0$, we take $R = 4$ to compute the dynamics by ChebCN, ChebExact and ADI for the following two cases

Case 1: (linear case) $\beta = 0$,
Case 2: (non-dipolar BEC) $\beta = 7$,

to investigate the effect of boundary condition on symmetry preservation performance.

To make errors coming from temporal and spatial discretization negligible, we choose $\Delta t = \pi/10^4$, and $N_x = N_y = 256$ for ADI scheme, $N_r = 320, N_\theta = 64$ for ChebCN/ChebExact scheme. The exact solution in **Case 1**, by Eq. (A.4), is

$$\psi(\mathbf{x}, T) = \psi_0(A(T)\mathbf{x}), \quad \mathbf{x} \in \mathbb{R}^2, \tag{3.46}$$

with

$$A(T) = \begin{pmatrix} \cos(\Omega T) & -\sin(\Omega T) \\ \sin(\Omega T) & \cos(\Omega T) \end{pmatrix}.$$
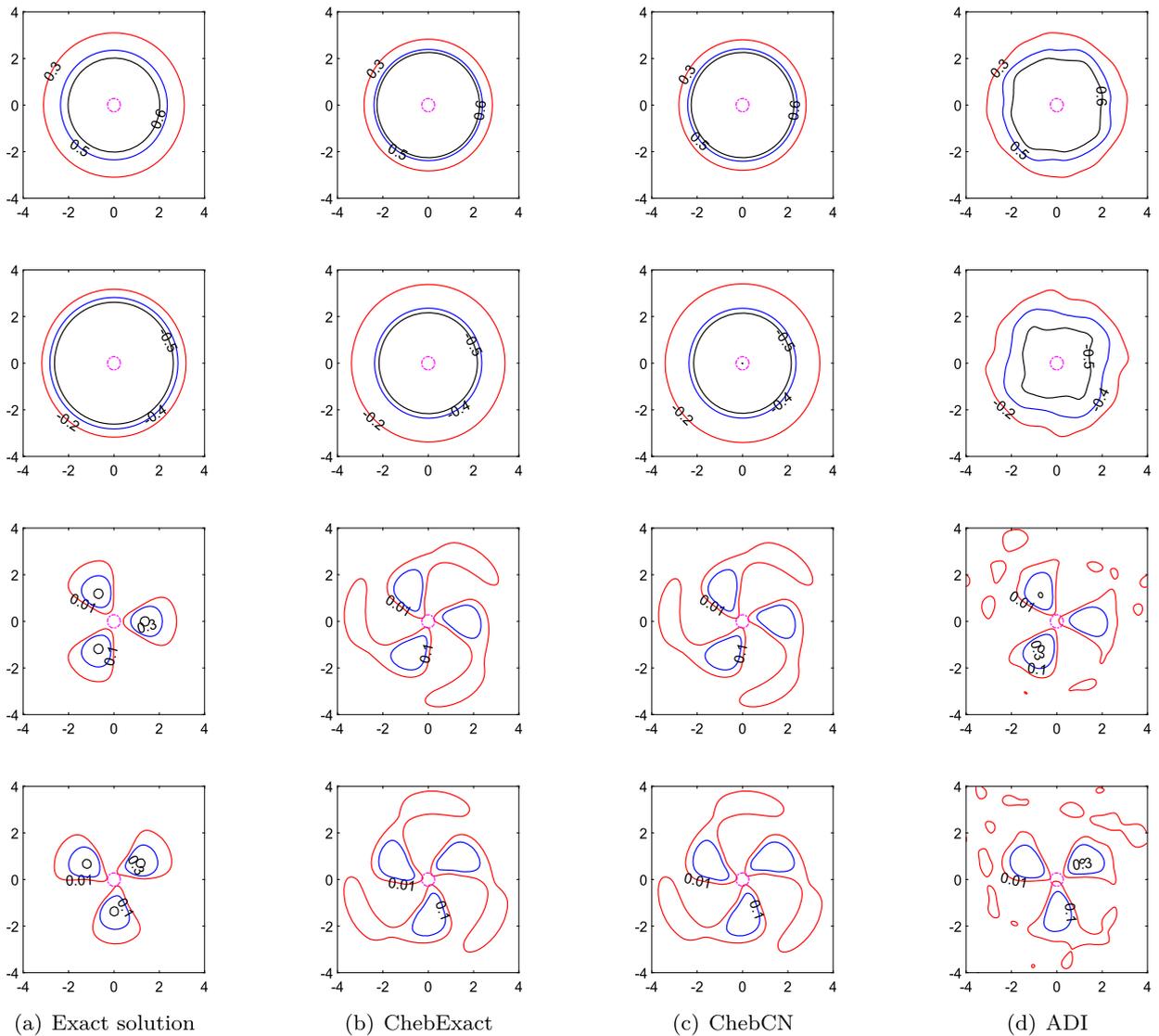
Fig. 5. Wave function (real part) at time $T = 2\pi$ for $\psi_0 = e^{-r^2/8}$ (top two rows) and $\psi_0 = (1 - e^{-r^2})e^{-r^2}(re^{i\theta})^3$ in **Example 4**. Odd (even) rows correspond to **Case 1** (**Case 2**) and the pink dotted line is the auxiliary circle in each image.

While in **Case 2**, the exact solution is computed by adopting rotating Lagrangian coordinates method [11] with $R = 16, N_x = N_y = 1024$ and $\Delta t = \pi/10^4$. Fig. 5 shows real part of the wave functions at time $T = 2\pi$ starting with initial values: Gauss ($e^{-r^2/8}$) and vortex of winding number 3, i.e., $(1 - e^{-r^2})e^{-r^2}(re^{i\theta})^3$.

It is clear that ChebCN and ChebExact perform better than ADI in preserving the rotational symmetry. Although all the wave functions differ from exact solution due to inexact boundary conditions, ChebCN and ChebExact are still able to keep the same rotational symmetry as the initial value, i.e., radial symmetry and $\pi/3$-rotational symmetry.

Example 5 *(Temporal integrator).* For rotating linear Schrödinger equation (1.1)-(1.3): $\beta = 0, \lambda = 0, \Omega = 1/3$, we take $\psi_0(\mathbf{x}) = e^{-|\mathbf{x}|^2}$ as the initial value to simulate its dynamics by ChebCN, ChebExact and ADI scheme, respectively.

We choose $R = 16$, and grids number $N_x = N_y = 256$ for ADI scheme, $N_r = 320, N_\theta = 64$ for ChebExact/ChebCN scheme to insure the spatial error can be neglected. Fig. 6 shows the images of wave function (real part) with fixed time step $\Delta t = \pi/12$ at final time $T = 80\pi$ when we can get the exact solution as Eq. (3.46). And Table 4 presents the temporary convergence of the three algorithms with the error function:

$$\mathcal{E}^{num}_{\Delta t} := \|\psi^{num}_{\Delta t} - \psi^{ext}\|_\infty \,/\, \|\psi^{ext}\|_\infty,$$

(a) Exact solution   (b) ChebExact   (c) ChebCN   (d) ADI
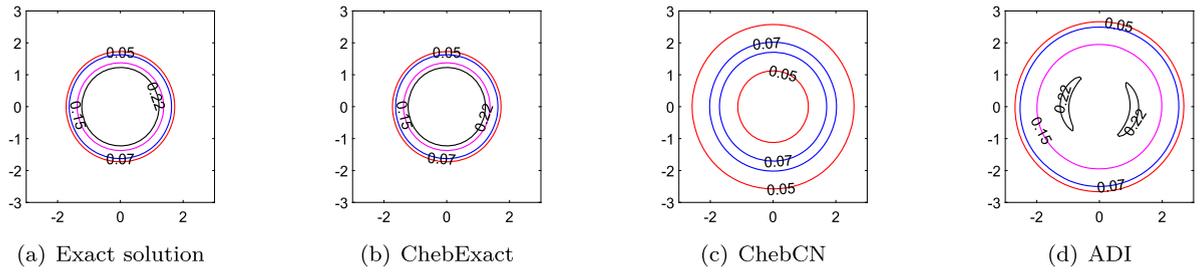
Fig. 6. Wave function (real part) at time $T = 80\pi$ for rotating linear Schrödinger equation in **Example 5**.

Table 4
Temporal convergence for rotating linear Schrödinger equation in Example 5.

		$\Delta t/\Delta t_0$ 1	1/2	1/4	1/8
ADI	$\mathcal{E}^{num}_{\Delta t}$	1.7647E-03	4.4103E-04	1.1025E-04	2.7561E-05
	Ord		2.0005	2.0001	2.0000
ChebCN	$\mathcal{E}^{num}_{\Delta t}$	4.2749E-02	1.2214E-02	3.1310E-03	7.8508E-04
	Ord		1.8074	1.9638	1.9957
ChebExact	$\mathcal{E}^{num}_{\Delta t}$	7.0275E-14	4.7243E-14	1.3172E-13	2.7204E-13

where ψ^{ext} is the exact solution and $\psi^{num}_{\Delta t}$ is the numerical solution. We replace $\psi^{num}_{\Delta t}$ with $\psi^{N_x,N_y}_{\Delta t}$ ($\psi^{N_r,N_\theta}_{\Delta t}$) for ADI (ChebCN/ChebExact) scheme, and the corresponding temporal convergence order is defined as (3.44) with $\mathcal{E}^{num}$ instead of $\mathcal{E}$. We set final time $T = 2\pi$ and remark $\Delta t_0 = 16\pi/1000$ in Table 4.

From Fig. 6, we can see that wave functions obtained by ADI and ChebCN differ from the exact solution, while wave function computed by ChebExact is almost identical to the exact solution. This phenomenon can be further confirmed by Table 4. In fact, ChebExact scheme is analytic in time, but ADI and ChebCN scheme are only second order accurate. Moreover, ChebCN preserves radial symmetry of the initial value.

3.4. Application

The time splitting Chebyshev-Fourier spectral method can be easily extended to related models, for example, the two-component rotating dipolar BEC, which is well described by following time-dependent two-dimensional nonlinear Schrödinger equation [35]

$$i\partial_t \psi_j(\mathbf{x},t) = \left[-\frac{1}{2}\nabla^2 + V_j(\mathbf{x}) - \Omega L_z + \sum_{k=1}^{2} (\beta_{jk}|\psi_k|^2 + \lambda_{jk}\,\varphi_k) \right] \psi_j(\mathbf{x},t), \quad t > 0, \tag{3.47}$$

$$\varphi_j(\mathbf{x},t) = \left(U * |\psi_j|^2 \right)(\mathbf{x},t), \qquad \mathbf{x} \in \mathbb{R}^2, \tag{3.48}$$

$$\psi_j(\mathbf{x},0) = \psi_j^0(\mathbf{x}), \qquad j = 1,2, \tag{3.49}$$

where $\psi_j(\mathbf{x},t)$ is the time-dependent wave function of the j-th component, β_{jk}, λ_{jk} represent the strength of inter-component local and nonlocal dipole-dipole interaction respectively. To simulate its dynamics, we adapt the ChebExact scheme to the above system, and choose to omit details as scheme adaptation is quite plain here.

Example 6. Consider the following function

$$f(\mathbf{x}) = \sum_{j=1}^{J} \left(1 - e^{-|\mathbf{x}-\mathbf{a}_j|^2} \right) e^{-|\mathbf{x}-\mathbf{a}_j|^2} \left((x - x_j) + i(y - y_j) \right)^k,$$

where $\mathbf{a}_j = (x_j, y_j)^T \in \mathbb{R}^2, j = 1, \dots, J$ are vortices centers, and $k \in \mathbb{N}$ is the winding number. We simulate Eq. (3.47)-(3.49) with the following two setups

    Case 1: (Two vortices) $J = 2, k = 1, \mathbf{a}_1 = (2,0)^T, \mathbf{a}_2 = (-2,0)^T$,
    Case 2: (Three vortices) $J = 3, k = 1, \mathbf{a}_1 = (0,2)^T, \mathbf{a}_2 = (1.61, -0.78)^T, \mathbf{a}_3 = (-1.61, -0.78)^T$.

The initial wave function for each component is chosen the same, i.e.,

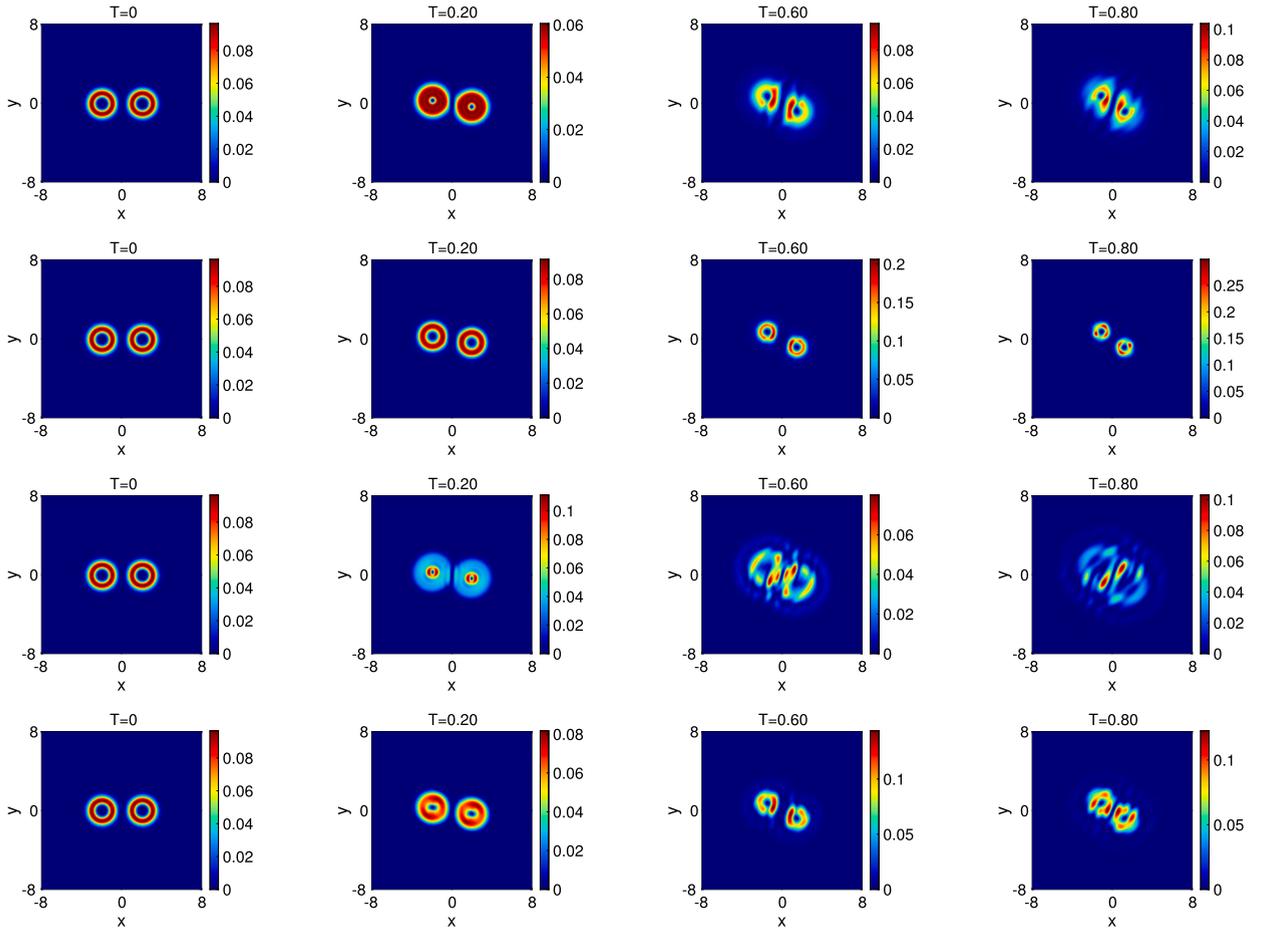$$\psi_1^0(\mathbf{x}) = \psi_2^0(\mathbf{x}) = f(\mathbf{x})/\|f\|_{L^2}. \tag{3.50}$$

Fig. 7. Density evolution of non-dipolar (top two rows) and dipolar BEC with **Case 1** setup in Example 6. Odd (even) rows correspond to component one (two).

The external trapping potentials are the same, i.e., $V_1(\mathbf{x}) = V_2(\mathbf{x}) = \frac{|\mathbf{x}|^2}{2}$. The other model parameters as chosen as $\Omega = 0.8$, $\beta_{11} = 40, \beta_{22} = -40, \beta_{12} = \beta_{21} = -20$, and the dipole orientation for each component is $\mathbf{n}_1 = (1/2, \frac{\sqrt{3}}{2}, 0)^T, \mathbf{n}_2 = (0, 0, 1)^T$. For both cases, we investigate the dipolar BEC, i.e., $\lambda_{12} = \lambda_{21} = 0.6\beta_{12}, \lambda_{ii} = 0.2\beta_{ii}$, and non-dipolar version, i.e., $\lambda_{ij} = 0, i, j = 1, 2$.

In computation, we take $\Delta t = 0.0001, R = 16$ and $N_r = 640, N_\theta = 128$. Figs. 7-8 illustrate the density evolution at different time, from which we can see clearly that the density of each component keeps the same symmetry property as its initial value for the non-dipolar BEC, while they change in anisotropic way for the dipolar BEC due to the anisotropy of DDI.

4. Conclusion

We have proposed a Chebyshev-Fourier spectral method to approximate the wave function of the rotating dipolar BEC within a disk, and construct a Chebyshev-Fourier-KTM method to compute the nonlocal dipolar potential. The Hamiltonian is split into linear operator, i.e., the Laplacian and rotation terms, and the nonlinear operator (the remaining terms). Each subproblem can be solved efficiently and accurately in either phase or physical space respectively. Based on operator splitting, we can easily construct high order spectral method to simulate the dynamics. Ample numerical results are presented to confirm the accuracy and efficiency for both nonlocal potential and the wave function, together with one application to a two-component dipolar rotating Bose-Einstein condensates. Moreover, we investigate the symmetry preserving property with a detailed comparison with existing scheme. Furthermore, the proposed method can be extended to 3D case. To approximate the wave function that is supported in a cylindrical domain, one may apply Chebyshev-Fourier spectral method in the polar coordinates, as we did in this paper, and Fourier spectral method in the z-direction. For a spherical domain, one may expand the wave function using spherical harmonics in the azimuthal and zenith variables and Chebyshev spectral method in the radial direction. In addition, the Kernel Truncation method and time splitting method can be easily applied with minimal modifications. In the future, we shall explore and develop the strategies to compute the dynamics of rotating dipolar BEC.
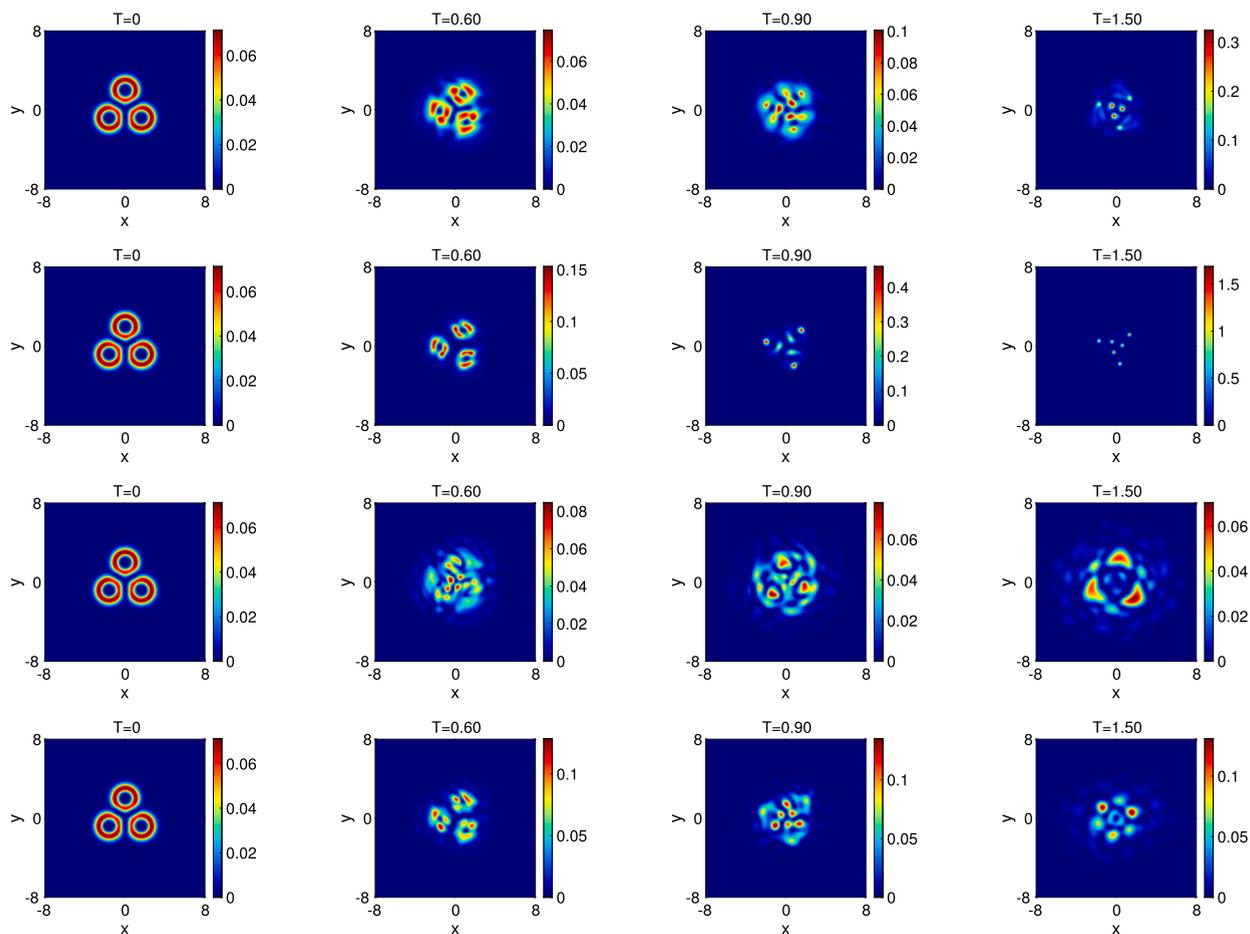
Fig. 8. Density evolution of non-dipolar (top two rows) and dipolar BEC with **Case 2** setup in Example 6. Odd (even) rows correspond to component one (two).

CRediT authorship contribution statement

Hanquan Wang: Funding acquisition, Methodology, Writing – review & editing. **Jing Wang:** Funding acquisition, Validation, Writing – review & editing. **Shaobo Zhang:** Data curation, Formal analysis, Methodology, Software, Validation, Visualization, Writing – original draft, Writing – review & editing. **Yong Zhang:** Conceptualization, Formal analysis, Funding acquisition, Methodology, Project administration, Resources, Supervision, Validation, Visualization, Writing – review & editing.

Declaration of competing interest

The authors declare that they have no known competing financial interests or personal relationships that could have appeared to influence the work reported in this paper.

Data availability

Data will be made available on request.

Acknowledgements

Appendix A. Exact solution for rotating linear Schrödinger equation

Theorem A.1. *Considering the rotating linear Schrödinger equation* (1.1)-(1.3), *i.e.,* $\beta = \lambda = 0$, *when the trapping potential is harmonic isotropic, i.e.,* $V(\boldsymbol{x}) = \frac{1}{2}\gamma^2|\boldsymbol{x}|^2$, *we can obtain the following analytical solution:*

$$\psi(\boldsymbol{x},t) = \sum_{m=0}^{\infty}\sum_{n=0}^{\infty} C_{mn} e^{-i\gamma t(m+n+1)}\hat{H}_n(\hat{x})\hat{H}_m(\hat{y}), \quad \boldsymbol{x} \in \mathbb{R}^2, \tag{A.1}$$

where $\boldsymbol{x} = \frac{A(t)^{-1}}{\sqrt{\gamma}}\hat{\boldsymbol{x}} = \frac{A(t)^{-1}}{\sqrt{\gamma}}(\hat{x},\hat{y})^T$ *with* $A(t)$ *(the rotational matrix) given below explicitly [11]*

$$A(t) = \begin{pmatrix} \cos(\Omega t) & -\sin(\Omega t) \\ \sin(\Omega t) & \cos(\Omega t) \end{pmatrix} \tag{A.2}$$

and C_{mn} *are the Fourier-Bessel expansion coefficients with respect to the orthonormal Hermite functions of the initial wave function [34], i.e.,*

$$C_{mn} = \int_{\mathbb{R}^2} \psi_0(\hat{\boldsymbol{x}}/\sqrt{\gamma})\hat{H}_n(\hat{x})\hat{H}_m(\hat{y})\, \mathrm{d}\hat{\boldsymbol{x}}. \tag{A.3}$$

Especially, for $\gamma t = 2k\pi$, $k \in \mathbb{Z}$, *the exact solution* (A.1) *can be simplified as*

$$\psi(\boldsymbol{x},t) = \psi_0(A(t)\boldsymbol{x}). \tag{A.4}$$

Proof. In the rotating Lagrangian coordinates $\tilde{\mathbf{x}} = A(t)\mathbf{x}$, we denote the wave function as $\Phi(\tilde{\mathbf{x}},t) := \psi(\mathbf{x},t)$ and derive

$$\partial_t \Phi(\tilde{\mathbf{x}},t) = \partial_t \psi(\mathbf{x},t) - \Omega(x\partial_y - y\partial_x)\psi(\mathbf{x},t), \tag{A.5}$$

$$\nabla\Phi = A(t)\nabla\psi, \quad \Delta\Phi = \Delta\psi, \quad V(\tilde{\mathbf{x}}) = V(\mathbf{x}) = \frac{1}{2}\gamma^2|\mathbf{x}|^2. \tag{A.6}$$

The original equation is then reformulated as follows

$$i\partial_t\Phi = \left[-\frac{1}{2}\Delta + \frac{1}{2}\gamma^2|\tilde{\mathbf{x}}|^2\right]\Phi(\tilde{\mathbf{x}},t), \text{ with initial value } \Phi(\tilde{\mathbf{x}},0) = \psi_0(\tilde{\mathbf{x}}).$$

Then by the change of variables $\hat{\mathbf{x}} = \sqrt{\gamma}\,\tilde{\mathbf{x}}$ and $\phi(\hat{\mathbf{x}},t) = \Phi(\tilde{\mathbf{x}},t)$, the above equation is rewritten as follows

$$i\partial_t\phi := \gamma\mathcal{L}\phi = \gamma\left[-\frac{1}{2}\Delta + \frac{1}{2}|\hat{\mathbf{x}}|^2\right]\phi(\hat{\mathbf{x}},t), \text{ with initial value } \phi(\hat{\mathbf{x}},0) = \psi_0(\hat{\mathbf{x}}/\sqrt{\gamma}).$$

As is known that the operator $\mathcal{L}$ admits the orthonormal Hermite functions $\hat{H}_n(\hat{x})\hat{H}_m(\hat{y})$ as eigenfunctions [34] with eigenvalues $m+n+1$, we obtain the following exact solution

$$\psi(\mathbf{x},t) = \phi(\hat{\mathbf{x}},t) = e^{-i\gamma t\mathcal{L}}\phi(\hat{\mathbf{x}},0) = \sum_{m=0}^{\infty}\sum_{n=0}^{\infty} C_{mn} e^{-i\gamma t(m+n+1)}\hat{H}_n(\hat{x})\hat{H}_m(\hat{y}). \tag{A.7}$$

Especially, for $\gamma t = 2k\pi$, $k \in \mathbb{Z}$, the exact solution is then simplified as

$$\psi(\mathbf{x},t) = \sum_{m=0}^{\infty}\sum_{n=0}^{\infty} C_{mn}\hat{H}_n(\hat{x})\hat{H}_m(\hat{y}) = \phi(\hat{\mathbf{x}},0) = \psi_0(A(t)\mathbf{x}). \quad \square$$

Appendix B. Rotational symmetry

Theorem B.1. *When the trapping potential and convolution kernel function are both isotropic, i.e.,* $V(\boldsymbol{x}) = V(|\boldsymbol{x}|)$ *and* $U(\boldsymbol{x}) = U(|\boldsymbol{x}|)$, *the rotating nonlocal NLSE* (1.1)-(1.3) *keeps fully rotational symmetry. That is, for solutions starting with initial value* $\psi_1^0(\boldsymbol{x})$ *and* $\psi_2^0(\boldsymbol{x}) = \psi_1^0(A\boldsymbol{x})$, *where* A *is the rotational matrix defined below*

$$A = \begin{pmatrix} \cos\alpha & -\sin\alpha \\ \sin\alpha & \cos\alpha \end{pmatrix}, \alpha \in [0, 2\pi],$$

$\psi_2(\boldsymbol{x},t)$ *is also a* α-*rotation of* $\psi_1(\boldsymbol{x},t)$, *i.e.,* $\psi_2(\boldsymbol{x},t) = \psi_1(A\boldsymbol{x},t)$.

Proof. We denote

$$\tilde{\mathbf{x}} = \begin{pmatrix} \tilde{x} \\ \tilde{y} \end{pmatrix} = A\mathbf{x} = \begin{pmatrix} x\cos\alpha - y\sin\alpha \\ x\sin\alpha + y\cos\alpha \end{pmatrix}, \quad \mathbf{x} = A^{-1}\tilde{\mathbf{x}},$$

and $\psi_2^0(\mathbf{x}) = \psi_1^0(\tilde{\mathbf{x}})$. Then we can derive

$$\partial_t \psi_2(\mathbf{x},t) = \partial_t \psi_1(\tilde{\mathbf{x}},t), \quad \Delta \psi_2(\mathbf{x},t) = \Delta \psi_1(\tilde{\mathbf{x}},t), \quad V(\mathbf{x}) = V(|A^{-1}\tilde{\mathbf{x}}|) = V(\tilde{\mathbf{x}}),$$

(B.1)

because of $|A^{-1}| = 1$. Using chain rule, we obtain

$$\partial_x \psi_2(\mathbf{x},t) = (\cos\alpha \cdot \partial_{\tilde{x}} + \sin\alpha \cdot \partial_{\tilde{y}})\psi_1(\tilde{\mathbf{x}},t), \quad \partial_y \psi_2(\mathbf{x},t) = (-\sin\alpha \cdot \partial_{\tilde{x}} + \cos\alpha \cdot \partial_{\tilde{y}})\psi_1(\tilde{\mathbf{x}},t).$$

Plugging them into $L_z \psi_2(\mathbf{x},t)$, we have

$$L_z \psi_2(\mathbf{x},t) = -i[(x\cos\alpha - y\sin\alpha)\partial_{\tilde{y}} - (x\sin\alpha + y\cos\alpha)\partial_{\tilde{x}}]\psi_1(\tilde{\mathbf{x}},t) = L_z \psi_1(\tilde{\mathbf{x}},t).$$

(B.2)

For the nonlocal potential $\varphi(\mathbf{x},t)$(1.2), substituting $\psi_2(\mathbf{y},t)$ for $\psi(\mathbf{y},t)$, we have

$$\varphi_2(\mathbf{x},t) = \int_{\mathbb{R}^2} U(\mathbf{x}-\mathbf{y})|\psi_2(\mathbf{y},t)|^2 \mathrm{d}\mathbf{y} = \int_{\mathbb{R}^2} U(A^{-1}(\tilde{\mathbf{x}}-\tilde{\mathbf{y}}))|\psi_1(\tilde{\mathbf{y}},t)|^2 \mathrm{d}\tilde{\mathbf{y}},$$

which can be reformulated as

$$\varphi_2(\mathbf{x},t) = \int_{\mathbb{R}^2} U(\tilde{\mathbf{x}}-\tilde{\mathbf{y}})|\psi_1(\tilde{\mathbf{y}},t)|^2 \mathrm{d}\tilde{\mathbf{y}} = \varphi_1(\tilde{\mathbf{x}},t).$$

(B.3)

Therefore, we can conclude that $\psi_2(\mathbf{x},t)$ satisfies the nonlinear Schrödinger equation (1.1)-(1.3), starting with the initial value $\psi_2^0(\mathbf{x}) = \psi_1^0(A\mathbf{x})$, that is, $\psi_2(\mathbf{x},t) = \psi_1(A\mathbf{x},t)$. $\quad\square$

Theorem B.2. *For non-dipolar rotating NLSE* (1.1)-(1.3) *under symmetric potential, i.e.,* $V(\mathbf{x}) = V(|\mathbf{x}|)$, *the time splitting Chebyshev-Fourier spectral method keeps rotational symmetry when the rotation angle α is an integer multiple of mesh size in the azimuthal direction, i.e.,* $\alpha \in \frac{2\pi}{N_\theta}\mathbb{Z}^+$.

Proof. For notations simplicity, we denote $\psi^n(r_p,\theta_q)$ as an approximation of the wave function at time t_n on the non-uniform mesh $\mathcal{T}$, i.e., $\psi(r_p,\theta_q,t_n)$. To confirm the α-symmetry, it suffices to prove that $\psi_2^{n+1}(r_p,\theta_q) = \psi_1^{n+1}(r_p,\theta_q+\alpha)$ when $\psi_2^n(r_p,\theta_q) = \psi_1^n(r_p,\theta_q+\alpha)$, where α is an integer multiple of mesh size.

As shown before, the numerical solution (also the exact solution) of the nonlinear subproblem (2.33) reads explicitly as

$$\begin{aligned}
\psi_2^{n+1}(r_p,\theta_q) &= e^{-i\Delta t\left(V(r_p)+\beta|\psi_2^n(r_p,\theta_q)|^2\right)}\psi_2^n(r_p,\theta_q) \\
&= e^{-i\Delta t\left(V(r_p)+\beta|\psi_1^n(r_p,\theta_q+\alpha)|^2\right)}\psi_1^n(r_p,\theta_q+\alpha) \\
&= \psi_1^{n+1}(r_p,\theta_q+\alpha).
\end{aligned}$$

For the linear subproblem (2.32), the numerical solution is reformulated as

$$\widehat{\Psi}_k^{n+1} = G\,\widehat{\Psi}_k^n, \quad \forall k = -\frac{N_\theta}{2},\ldots,\frac{N_\theta}{2}-1,$$

where the matrix G is independent of initial wave function. Since $\psi_2^n(r_p,\theta_q) = \psi_1^n(r_p,\theta_q+\alpha)$, then for $\alpha \in \frac{2\pi}{N_\theta}\mathbb{Z}^+$, we derive the following identity

$$\widetilde{\psi}_{2,k}^n(r_p) = e^{ik\alpha}\,\widetilde{\psi}_{1,k}^n(r_p),$$

which implies

$$\widehat{\Psi}_{2,k}^{n+1} = G\,\widehat{\Psi}_{2,k}^n = G\,e^{ik\alpha}\widehat{\Psi}_{1,k}^n = e^{ik\alpha}(G\widehat{\Psi}_{1,k}^n) = e^{ik\alpha}\widehat{\Psi}_{1,k}^{n+1}.$$

(B.4)

It is clear that the identity $\psi_2^{n+1}(r_p,\theta_q) = \psi_1^{n+1}(r_p,\theta_q+\alpha)$ holds true for the linear subproblem (2.32). Since both linear and nonlinear solvers keep rotational symmetry, the time splitting Chebyshev-Fourier spectral method keeps rotational symmetry. $\quad\square$

Appendix C. Error estimate of Chebyshev-Fourier-Kernel Truncation method

Here we shall present the error analysis of Chebyshev-Fourier KTM for nonlocal potential, whose error originally comes from the approximation of the density function. To quantify the error estimate, we define the following norm

$$\|\varphi - \varphi_N\|_{\infty,B_R} := \|\varphi - \varphi_N\|_{L^\infty(B_R)} = \sup_{\mathbf{x}\in B_R} |(\varphi - \varphi_N)(\mathbf{x})|,$$

where $\varphi_N(\mathbf{x}) = \int_{B_{2R}} U(\mathbf{y})\rho_N(\mathbf{x}-\mathbf{y})\mathrm{d}\mathbf{y}$ is the approximation of function $\varphi(\mathbf{x})$. For notations simplicity, we take the same grids number in x and y directions, and denote $\mathcal{T}_{rect}^{2R}$ as a uniform mesh grids by a simple substitution of $(2R, 2N, 2N)$ for (R, N_x, N_y) in Eq. (2.25). $\rho_N(\mathbf{x})$ is the Fourier interpolation function on $\mathcal{D}_{2R}$ with source grid values $\rho_{j_1,j_2}^{CF} := \rho^{CF}(x_{j_1}, y_{j_2})$ on $\mathcal{T}_{rect}^{2R}$, where $\rho^{CF}(\mathbf{x}) = P(\mathbf{x})$

(Eq. (2.16)-(2.18)) with a substitution of ρ for ψ when $\mathbf{x} \in \mathcal{B}_R$ and $\rho^{CF}(\mathbf{x}) = 0$ for others. We use $A \lesssim B$ to denote $A \leq c B$ where the constant $c > 0$ is independent of the grid number.

Theorem C.1. *For smooth and compactly supported function $\rho(\mathbf{x})$, assuming that $\mathrm{supp}\{\rho\} \subsetneq \mathcal{B}_R$ and $\rho(\cdot, \theta)$ is analytic on $r \in [0, R]$, then the following estimate*

$$\|\varphi - \varphi_N\|_{\infty, \mathcal{B}_R} \lesssim N^{-(m-1)} + N^2 \left(N_\theta^{-(m_\theta - 1/2)} + \frac{N_\theta}{L^{N_r} - 1} \right), \tag{C.1}$$

with constant $L > 1$ holds true for any $m > 1$ and $m_\theta > 1/2$, where m and m_θ indicate the regularity of ρ on Cartesian coordinates and in the θ direction, respectively.

Proof. To estimate the errors, we have

$$|(\varphi - \varphi_N)(\mathbf{x})| = |\int_{\mathbf{B}_{2R}} U(\mathbf{y})(\rho - \rho_N)(\mathbf{x} - \mathbf{y})\mathrm{d}\mathbf{y}|$$

$$\leq \max_{\substack{\mathbf{x} \in \mathcal{B}_R \\ \mathbf{y} \in \mathcal{B}_{2R}}} |(\rho - \rho_N)(\mathbf{x} - \mathbf{y})| \int_{\mathbf{B}_{2R}} U(\mathbf{y})\mathrm{d}\mathbf{y} \lesssim \|\rho - \rho_N\|_{\infty, \mathbf{B}_{3R}}.$$

Taking supremum with respect to $\mathbf{x}$ and using the periodicity of ρ_N (similar to [28]), we obtain

$$\|\varphi - \varphi_N\|_{\infty, \mathcal{B}_R} \lesssim \|\rho - \rho_N\|_{\infty, \mathbf{D}_{3R}} = \|\rho - \rho_N\|_{\infty, \mathbf{D}_{2R}}. \tag{C.2}$$

By introducing the Fourier interpolation function ρ^M, whose source grid values are ρ_{j_1, j_2} on $\mathcal{T}_{rect}^{2R}$, we apply the error estimates of Fourier spectral method [34,28] and then obtain

$$\|\rho - \rho_N\|_{\infty, \mathbf{D}_{2R}} \leq \|\rho - \rho^M\|_{\infty, \mathbf{D}_{2R}} + \|\rho^M - \rho_N\|_{\infty, \mathbf{D}_{2R}}$$

$$\lesssim N^{-(m-1)} |\rho|_{m, \mathcal{B}_R} + \|\rho^M - \rho_N\|_{\infty, \mathbf{D}_{2R}}, \tag{C.3}$$

where $|\cdot|_{m, \mathcal{B}_R}$ is the semi-norm in Hilbert spaces $H^m(\mathcal{B}_R)$. In addition, the last term in Eq. (C.3) can be rewritten as

$$\|\rho^M - \rho_N\|_{\infty, \mathbf{D}_{2R}} \leq \sum_{k_1 = -N}^{N-1} \sum_{k_2 = -N}^{N-1} \sum_{j_1 = 0}^{2N-1} \sum_{j_2 = 0}^{2N-1} \frac{1}{(2N)^2} |\rho_{j_1, j_2} - \rho_{j_1, j_2}^{CF}| \leq 4N^2 \|\rho - \rho^{CF}\|_{\infty, \mathbf{B}_R}. \tag{C.4}$$

Similar to Eq. (C.3), we introduce the function ρ^F on $\mathbf{B}_R$, which is defined as

$$\rho^F(\mathbf{x}) = \sum_{k = -N_\theta/2}^{N_\theta/2 - 1} \widetilde{\rho}_k(r) e^{ik\theta} \quad \text{with} \quad \widetilde{\rho}_k(r) = \frac{1}{N_\theta} \sum_{j=1}^{N_\theta - 1} \rho(r, \theta_j) e^{-ik\theta_j},$$

and then we obtain

$$\|\rho - \rho^{CF}\|_{\infty, \mathbf{B}_R} \lesssim N_\theta^{-(m_\theta - 1/2)} \max_{r \in [0, R]} \{|\rho|_{m_\theta, [0, 2\pi]}(r)\} + \|\rho^F - \rho^{CF}\|_{\infty, \mathbf{B}_R}. \tag{C.5}$$

By exchanging the summation order, we obtain

$$\rho^F - \rho^{CF} = \frac{1}{N_\theta} \sum_{j=0}^{N_\theta - 1} \left[\left(\rho(r, \theta_j) - \rho^C(r, \theta_j) \right) \left(\sum_{k=-N_\theta/2}^{N_\theta/2 - 1} e^{ik(\theta - \theta_j)} \right) \right],$$

where $\rho^C(r, \theta_j)$ is the Chebyshev interpolation for $\rho(r, \theta_j)$. According to error estimates of Chebyshev spectral method [39], we obtain

$$\|\rho^F - \rho^{CF}\|_{\infty, \mathbf{B}_R} \leq \sum_{j=0}^{N_\theta - 1} \| \left(\rho(r, \theta_j) - \rho^C(r, \theta_j) \right) \|_{\infty, [0, R]} \lesssim \frac{N_\theta}{L^{N_r} - 1}. \tag{C.6}$$

Thus Eq. (C.1) is proved. $\square$

References

[1] J.R. Abo-Shaeer, C. Raman, J.M. Vogels, W. Ketterle, Observation of vortex lattices in Bose-Einstein condensates, Science 292 (2001) 476–479.

[2] M.H. Anderson, J.R. Ensher, M.R. Matthewa, C.E. Wieman, E.A. Cornell, Observation of Bose-Einstein condensation in a dilute atomic vapor, Science 269 (1995) 198–201.

[3] X. Antoine, W. Bao, C. Besse, Computational methods for the dynamics of the nonlinear Schrödinger/Gross-Pitaevskii equations, Comput. Phys. Commun. 184 (2013) 2621–2633.

[4] X. Antoine, A. Levitt, Q. Tang, Efficient spectral computation of the stationary states of rotating Bose-Einstein condensates by preconditioned nonlinear conjugate gradient methods, J. Comput. Phys. 343 (2017) 92–109.

[5] X. Antoine, Q. Tang, Y. Zhang, A preconditioned conjugated gradient method for computing ground states of rotating dipolar Bose-Einstein condensates via kernel truncation method for dipole-dipole interaction evaluation, Commun. Comput. Phys. 24 (4) (2018) 966–988.

[6] W. Bao, Y. Cai, Mathematical theory and numerical methods for Bose-Einstein condensation, Kinet. Relat. Models 6 (2013) 1–135.

[7] W. Bao, Y. Cai, H. Wang, Efficient numerical methods for computing ground states and dynamics of dipolar Bose-Einstein condensates, J. Comput. Phys. 229 (2010) 7874–7892.

[8] W. Bao, Q. Du, Y. Zhang, Dynamics of rotating Bose-Einstein condensates and its efficient and accurate numerical computation, SIAM J. Appl. Math. 66 (2006) 758–786.

[9] W. Bao, S. Jiang, Q. Tang, Y. Zhang, Computing the ground state and dynamics of the nonlinear Schrödinger equation with nonlocal interactions via the nonuniform FFT, J. Comput. Phys. 296 (2015) 72–89.

[10] W. Bao, H. Li, J. Shen, A generalized-Laguerre-Fourier-Hermite pseudospectral method for computing the dynamics of rotating Bose-Einstein condensates, SIAM J. Sci. Comput. 31 (5) (2009) 3685–3711.

[11] W. Bao, D. Marahrens, Q. Tang, Y. Zhang, A simple and efficient numerical method for computing the dynamics of rotating Bose-Einstein condensates via rotating Lagrangian coordinates, SIAM J. Sci. Comput. 35 (6) (2013) 2671–2695.

[12] W. Bao, Q. Tang, Y. Zhang, Accurate and efficient numerical methods for computing ground states and dynamics of dipolar Bose-Einstein condensates via the nonuniform FFT, Commun. Comput. Phys. 19 (5) (2016) 1141–1166.

[13] W. Bao, H. Wang, An efficient and spectrally accurate numerical method for computing dynamics of rotating Bose-Einstein condensates, J. Comput. Phys. 271 (2006) 612–626.

[14] C. Besse, G. Dujardin, I. Lacroix-Violet, High order exponential integrators for nonlinear Schrödinger equations with application to rotating Bose-Einstein condensates, SIAM J. Numer. Anal. 55 (3) (2017) 1387–1411.

[15] C.C. Bradley, C.A. Sackett, J.J. Tollett, R.G. Hulet, Evidence of Bose-Einstein condensation in an atomic gas with attractive interactions, Phys. Rev. Lett. 75 (1995) 1687–1690.

[16] B.M. Caradoc-Davis, R.J. Ballagh, K. Burnett, Coherent dynamics of vortex formation in trapped Bose-Einstein condensates, Phys. Rev. Lett. 83 (1999) 895–898.

[17] A. Cerioni, L. Genovese, A. Mirone, V. Sole, Efficient and accurate solver of the three-dimensional screened and unscreened Poisson's equation with generic boundary conditions, J. Chem. Phys. 137 (2012) 134108.

[18] K.B. Davis, M.O. Mewes, M.R. Andrews, N.J. van Druten, D.S. Durfee, D.M. Kurn, W. Ketterle, Bose-Einstein condensation in a gas of sodium atoms, Phys. Rev. Lett. 75 (1995) 3969–3973.

[19] L. Exl, N.J. Mauser, Y. Zhang, Accurate and efficient computation of nonlocal potentials based on Gaussian-sum approximation, J. Comput. Phys. 327 (2016) 629–642.

[20] X. Feng, B. Li, S. Ma, High-order mass- and energy-conserving SAV-Gauss collocation finite element methods for the nonlinear Schrödinger equation, SIAM J. Numer. Anal. 59 (2021) 1566–1591.

[21] I. Ferrier-Barbut, H. Kadau, M. Schmitt, M. Wenzel, T. Pfau, Observation of quantum droplets in a strongly dipolar Bose gas, Phys. Rev. Lett. 116 (2016) 215301.

[22] L. Greengard, S. Jiang, Y. Zhang, The anisotropic truncated kernel method for convolution with free-space Green's functions, SIAM J. Sci. Comput. 40 (2018) A3733–A3754.

[23] A. Griesmaier, J. Werner, S. Hensler, J. Stuhler, T. Pfau, Bose-Einstein condensation of chromium, Phys. Rev. Lett. 94 (2005) 160401.

[24] S. Jiang, L. Greengard, W. Bao, Fast and accurate evaluation of nonlocal Coulomb and dipole-dipole interaction via the nonuniform FFT, SIAM J. Sci. Comput. 36 (2014) B777–B794.

[25] M. Kobayashi, P. Parnaudeau, F. Luddens, C. Lothodé, L. Danaila, M. Brachet, I. Danaila, Quantum turbulence simulations using the Gross–Pitaevskii equation: high-performance computing and new numerical benchmarks, Comput. Phys. Commun. 258 (2021) 107579.

[26] T. Lahaye, C. Menotti, L. Santos, M. Lewenstein, T. Pfau, The physics of dipolar bosonic quantum gases, Rep. Prog. Phys. 72 (2009) 126401.

[27] B. Li, Y. Wu, A fully discrete low-regularity integrator for the 1D periodic cubic nonlinear Schrödinger equation, Numer. Math. 149 (2021) 151–183.

[28] X. Liu, Q. Tang, S. Zhang, Y. Zhang, On optimal zero-padding of kernel truncation method, arXiv:2209.12180.

[29] N.J. Mauser, Y. Zhang, Exact artificial boundary condition for the Poisson equation in the simulation of the 2D Schrödinger-Poisson system, Commun. Comput. Phys. 16 (3) (2014) 764–780.

[30] N.J. Mauser, Y. Zhanga, X. Zhao, On the rotating Klein-Gordon equation for cosmic superfluid: non-relativistic limit and numerical methods, SIAM Multiscale Model. Simul. 18 (2) (2020) 999–1024.

[31] X. Meng, Q. Tang, Y. Zhang, A compact splitting method of the spin-1 Bose-Einstein condensates, preprint.

[32] J. Cao, B. Li, Y. Lin, A new second-order low-regularity integrator for the cubic nonlinear Schrödinger equation, IMA J. Numer. Anal. (2023), https://doi.org/10.1093/imanum/drad017.

[33] J. Shen, Efficient spectral-Galerkin methods III: polar and cylindrical geometries, SIAM J. Sci. Comput. 18 (1997) 1583–1604.

[34] J. Shen, T. Tang, L.-L. Wang, Spectral Methods: Algorithms, Analysis and Applications, Springer, 2011.

[35] Q. Tang, N. Mauser, Y. Zhang, A robust and efficient numerical method to compute the dynamics of the rotating two-component dipolar Bose-Einstein condensates, Comput. Phys. Commun. 219 (2017) 223–235.

[36] F. Vico, L. Greengard, M. Ferrando, Fast convolution with free-space Green's functions, J. Comput. Phys. 323 (2016) 191–203.

[37] M. Xia, S. Shao, T. Chou, Efficient scaling and moving techniques for spectral methods in unbounded domains, SIAM J. Sci. Comput. 43 (5) (2021) A3244–A3268.

[38] H. Yoshida, Construction of higher order symplectic integrators, Phys. Lett. A 150 (1990) 262–268.

[39] Z. Zhang, Superconvergence points of polynomial spectral interpolation, SIAM J. Numer. Anal. 50 (2012) 2966–2985.